

**HOLOGRAPHIC FABRICATION OF WOODPILE TYPE PHOTONIC CRYSTAL
TEMPLATES BY THE USE OF ONE-DIMENSIONAL DIFFRACTIVE OPTICAL
ELEMENTS**

by

Zsolt L. Poole

BS. In Electrical Engineering, University of Pittsburgh, 2005

Submitted to the Graduate Faculty of
Swanson School of Engineering in partial fulfillment
of the requirements for the degree of
Master of Science in Electrical Engineering

University of Pittsburgh

2009

UNIVERSITY OF PITTSBURGH
SWANSON SCHOOL OF ENGINEERING

This thesis was presented

by

Zsolt L. Poole

It was defended on

Nov. 30th, 2009

and approved by

Joel Falk, PhD, Professor

William Stanchina, PhD, Professor and Chairman

Guangyong Li, PhD, Assistant Professor

Thesis Advisor: Kevin P. Chen, PhD, Associate Professor

Copyright © by Zsolt L. Poole

2009

ABSTRACT

HOLOGRAPHIC FABRICATION OF WOODPILE TYPE PHOTONIC CRYSTAL TEMPLATES BY THE USE OF ONE-DIMENSIONAL DIFFRACTIVE OPTICAL ELEMENTS

Zsolt L. Poole, M.S

University of Pittsburgh, 2009

As the search for fabrication techniques towards the production of large area defect free three-dimensional photonic crystals continues, holographic lithography presents itself as a possible solution. In this thesis, a simplified method that is free of complex optical setups is demonstrated. Within the core of the method presented lies a readily available optical component, a phase grating that by design presents a region of interference available for lithographic processing. The phase grating exhibiting a one-dimensional periodic arrangement designed to diffract into three substantial orders necessitates two exposures after which a three-dimensional periodic arrangement is realized. The negative tone photo resist, SU-8 utilized to record the designed intensity distribution proves itself as a viable intermediary towards high dielectric contrast structures.

The previously established large bandgap photonic crystals present fabrication challenges and thus approximations to these structures have been proposed. The specific method employed opens the door to only one of the previously established champion photonic crystals but nevertheless the most sought after diamond structure predicted to exhibit one of the largest possible band gaps. The woodpile structure possessing some of the qualities of the diamond

lattice is proven to be an adequate practical approximation and once properly designed exhibit large band gaps. The specific technique employed permits the exploration of the 11 FCC space groups along with the FCT and Tetragonal space groups.

The fascination that these structures have provoked is fueled by the vast predicted applications encompassing nearly all known scientific disciplines. One does not have to venture far to realize the potential held for the telecommunication industry such as dense wavelength multiplexers, high efficiency lasers, lasers of previously unavailable wavelengths, super continuum sources, flat lenses, superprisms, lossless waveguides, and resonant cavities to mention a few. Developments of these devices would progress the advancement of technologies such as optical storage, drug delivery systems, and advanced imaging. Some have even compared the discovery of these materials to the revolution achieved by the semiconductor industry with the advent of controllable electronic band gaps.

TABLE OF CONTENTS

ACKNOWLEDGEMENTS	X
1.0 INTRODUCTION.....	1
2.0 BACKGROUND INFORMATION	4
2.1 PBG THEORY AND CHARACTERISTICS	4
2.2 MAXWELL’S EQUATIONS IN PERIODIC STRUCTURES.....	9
2.2.1 Fourier expansion of the Permittivity	15
2.3 GENERATION OF THE INTERFERENCE PATTERN	25
2.3.1 Intensity Distribution Design.....	31
2.4 CRYSTALLOGRAPHIC ANALYSIS	35
2.5 SOLVING THE WAVE EQUATION	40
2.6 DRIVING CHEMISTRY	46
3.0 EXPERIMENTAL PROCEDURES	50
3.1 EXPERIMENT SETUP	50
3.2 FABRICATION PROCEDURE.....	54
4.0 EXPERIMENTAL RESULTS.....	56
4.1 STANDARD EVALUATION	56
4.2 DIFFRACTION ANALYSIS.....	61
5.0 ANALYSIS	63

5.1	SUMMARY	63
5.2	FUTURE WORK.....	67
APPENDIX A. UNION OPERATION FOR OBJECTS.....		70
APPENDIX B. MATLAB CODE THAT PREDICTS THE GEOMETRY OF THE STRUCTURE.....		72
APPENDIX C. MATLAB CODE THAT SOLVES FOR THE DISPERSION RELATION		75
APPENDIX D. SAMPLE MPB CODE USED FOR THE PREDICTION OF THE DISPERSION RELATIONS		82
BIBLIOGRAPHY		85

LIST OF FIGURES

Figure 1. Dispersion relation example, (a) band diagram of a uniform slab, (b) band diagram of a 1D periodic structure.....	5
Figure 2. Band opening demonstration by solution decoupling	6
Figure 3. Orientation of k-vectors for light diffracted by the phase grating.....	29
Figure 4. Normalized intensity distribution depicting the interference pattern generated by the phase grating.....	32
Figure 5. Normalized intensity distribution for two orthogonal exposures	33
Figure 6. Diagram depicting the two atoms in the primitive cell along the respective orientations	36
Figure 7. Evolution of the first Brillouin zone with changes in periodicity ratios	38
Figure 8. First Brillouin zone for a woodpile structure with $C/L=2^{1/2}$	39
Figure 9. The first Brillouin zone for a 60° structure (left), with top view to show the respective angular distortion (right)	40
Figure 10. Band structures of a woodpile arrangement with $C/L=1$, radii = $C/8$. (a)-the band structure by Matlab with cylindrical atoms, (b)-by MPB with cylindrical atoms, (c)-by MPB with rectangular atoms, and (d)-First Brillouin zone with labeled k-vectors.	44
Figure 11. The variations in bandgap with changes in periodicity ratios for the two exposure rotations.....	46
Figure 12. A general scheme for photosensitized cationic polymerization. Redrawn from Ref. ³³	48
Figure 13. Diagram of the light intensity present in the region of interference with separated components into DC and oscillating terms. Redrawn from Ref. ³³	49

Figure 14. Experimental setup used to exposure samples to designed interference.....	51
Figure 15. Surface SEM image of sample having 60° structure.....	57
Figure 16. Sideview SEM image (left) showing partial opening, Surface optical microscope image (right) showing excellent surface structure	57
Figure 17. SEM image of 60° structure, left close examination of the surface, right examination of the side	58
Figure 18. SEM image showing fully opened crystal with surface view (right) and side view (left).....	59
Figure 19. Surface image showing long range order (top left), closer view with predicted structure inset (top right), side view with prediction inset (bottom left), top view for another crystal plane (bottom right).....	60
Figure 20. Diffraction image taken for 90° structure with a HeNe laser (left) and white light (right).....	61
Figure 21. Diffraction image taken for 60° structure with a HeNe laser (left) and white light (right).....	62
Figure 22. Diffraction image taken for 45° structure with a HeNe laser (left) and white light (right).....	62

ACKNOWLEDGEMENTS

The continuous financial and academic support received from Dr. Kevin Chen made this research possible and I would be remiss if I did not recognize his encouragement. I would like to acknowledge the support I received from Dr. Joel Falk by allowing the use of his equipment and laboratory for this experiment along with assistance in theoretical analysis. Some deviations taken with the experiment led to the use of Dr. Albert Heberle's equipment and assistance for which I am grateful. The help I received from Dr. Steven Jacobs, as he helped with a problem I have encountered in developing the Fourier transforms, allowed me to establish a complete analytical description of the task at hand for which I am grateful. The support I have received from Ms. Sandra Weisberg in form of professional advice and personal encouragement along with assistance ensuring that I received financial aid in form of fellowships and assistantships was paramount throughout my graduate career. I would like to thank the University of Pittsburgh for providing me with Teaching Assistantships for the duration of my graduate study. I would be remiss if I did not mention the help I received from my four lab mates. Di Xu's theoretical and experimental assistance led to the success of the project. My discussions with Michael Buric, Chuck Jewart, and Ben McMillen and their assistance in analysis were integral to my success. Lastly, I would like to thank my family and friends for always encouraging me to succeed. Without their support, none of this would have been possible.

1.0 INTRODUCTION

The study of electromagnetic waves in dielectric materials in a periodic arrangement began over a century ago. The behavior of electromagnetic waves in these peculiar materials was first examined by Lord Rayleigh in 1887 in connection with the strange reflective properties of a certain crystalline mineral that has periodic planes at which twinning occur.¹ He concluded that these structures exhibit a narrow range of frequencies prohibiting the propagation of electromagnetic radiation and that this gap is dependent on the angle at which the light beams entered the media. The varying periodicity experienced by radiation impinging at non-orthogonal incidence lead to his observation of reflected colors highly dependent on this angle. A modern examination of these structures groups them into the familiar 1D photonic prystals along with their unique properties.

Following his work over the next century, considerable effort has been given to the study of multilayer films and has been put to use in many applications ranging from antireflection coatings to enhancing the efficiency of LEDs to highly reflective mirrors in laser cavities (VCSEL). It was not until 1987 when S. John and E. Yablonovitch, by their merging of electromagnetism and solid state physics, shed light on the concept of omnidirectional band gaps in two and three dimensions.^{2,3} These novel arrangements generated great interest and henceforth many developments have been made towards the fabrication and application of these

materials, later termed “photonic crystals.” Due to the difficulty of fabrication in the optical regime, early works were constrained to theoretical studies and structures in the microwave regime. In 1996, T. Krauss demonstrated the first two-dimensional photonic crystal at near-infrared wavelengths by borrowing fabrication methods used in the semiconductor industry.⁴ Despite the success of these developments, the first two-dimensional photonic crystal that found commercial interest was in the form of photonic crystal fiber, developed by P. Russell in 1998. The well established fabrication methods in the semiconductor industry expedited the developments of two-dimensional photonic crystals however this was not the case for the three-dimensional counterpart. The lack of available techniques to rely on led to slow progression in developments of three-dimensional crystal and an attempt was made by borrowing existing methods available in the semiconductor industry along with some clever thinking which led to the layer-by-layer fabricated woodpile structure.^{5,6}

The exhaustion of the available techniques and the difficulty that accompanied them led to the advancement of new and creative processes encompassing colloidal self-assembly⁷, multiphoton direct laser writing⁸, and multibeam holographic lithography⁹⁻¹⁶. Among the available techniques towards the fabrication of three-dimensional photonic crystals, holographic lithography has attracted the most attention for its inherent flexibility. Although its employment produces intermediary templates by the use of infiltration and inversion techniques,¹⁷ these can be converted into high dielectric contrast structures. Traditionally, multi beam interference lithography was realized by a large number of bulk optical components, such as mirrors, beam splitters, and lenses.^{10,11} These optical setups inherit many degrees of freedom demanding precision in alignment and are susceptible to thermal variations and mechanical vibrations. Recently, a number of groups have demonstrated the construction of multi beam interference

using single deflective or diffractive optical elements¹²⁻¹⁵ along with lithography based on multiple diffractive elements on one glass mask¹² and a single flat top prism.¹³ By employing two orthogonally aligned phase masks, photonic crystals with woodpile structures have been recently demonstrated through one or two laser exposures.¹⁴⁻¹⁶ Continuous attempts at reducing the components required either by utilizing more complex elements or by the merging of multiple elements into single components eased the battle with alignment stemming from thermal variations and mechanical vibrations and phase matching requirements of multiple overlapping beams. These advancements are not free from the constrictions that accompany them as these optical setups possessing reduced degrees of freedom are also limited to a half-space. That is, one side is used for the generation of the interference and the other is for the recording of the interference, thus resulting in elongation along the optic axis accompanied by reduced crystal symmetry and band gaps. The work presented here demonstrates the feasibility of producing large area defect free photonic crystal templates using diffractive optical elements as a replacement to bulk optical setups along with an attempt to regain lost crystal symmetry due to elongation.

2.0 BACKGROUND INFORMATION

2.1 PBG THEORY AND CHARACTERISTICS

Photonic crystals, structures composed of alternating high and low index of refraction, generally but not limited to dielectrics, arranged in some periodic scheme are theorized and have been demonstrated to exhibit unique characteristics that present a newfound control over electromagnetic radiation. Analogous to its electronic counterpart, atoms or molecules arranged in a repeating scheme present a periodic potential to a propagating electron. For electrons, the material and the geometric arrangement directly affect the conduction properties of the crystal. Electrons traversing conducting crystals without scattering posed a problem that the physics of the era was not equipped to handle, but this peculiar behavior was explained by the advent of the theory of quantum mechanics. This new physics treated the electrons as waves, and waves that met a specific criterion could traverse through a periodic potential without scattering; conversely, the structure could exhibit an energy gap that prohibits the propagation of these waves in a range of frequencies. Photonic crystals in which the constituents are replaced by macroscopic media with differing dielectric contrast and the periodic potential is replaced by a periodic dielectric function can present many of the same phenomena to photons as semiconductors do to electrons.

These novel artificial materials can provide exact control over the propagation of electromagnetic radiation. Once designed to fulfill a certain dielectric contrast requirement, they can prohibit the propagation of light in a range of frequencies along certain direction or all directions. Forbidden gaps in Photonic crystals can be either omnidirectional or partial, encompassing all possible directions of propagation or just a subset of wavevectors. Regardless of the span of the gap, the origin of the opening can be understood by examining a one-dimensional periodic system. A slab of dielectric with a uniform dielectric constant has plane wave eigensolutions $\omega(k)=ck$ referred to as the “light cone.” This system is a special case of periodic structures where period of repetition “a” approaches zero yielding the unbounded dispersion relation. Labeling the states in terms of Bloch envelope functions and wavevectors for some $a>0$, reveals the degeneracy inherent in this system. The wavevectors, $|k|>\pi/a$ are folded into the first Brillouin zone (dashed line in figure 1(a)), the $k=-\pi/a$ mode lies at an equivalent wavevector to the π/a mode with the same frequency and so on.

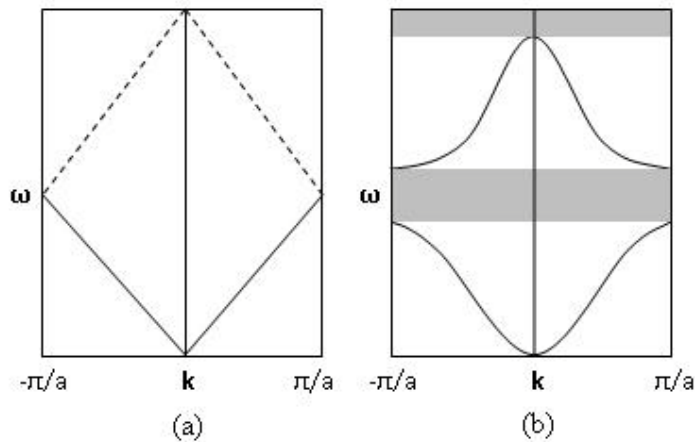


Figure 1. Dispersion relation example, (a) band diagram of a uniform slab, (b) band diagram of a 1D periodic structure.

A direct way of observing the origin of the opening of forbidden gaps is accomplished by decomposing the wave solutions into linear combinations of sines and cosines and disturbing the uniform dielectric function with a periodic component whether the disturbance is sinusoidal $\epsilon(x)=1+\Delta\cos(2\pi x/a)$, or some other oscillatory function.

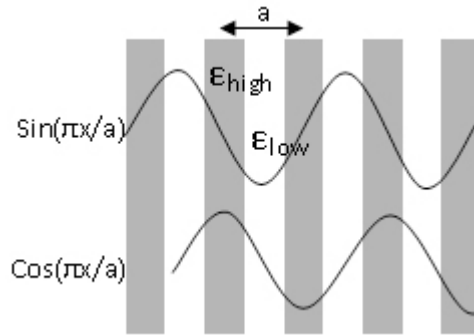


Figure 2. Band opening demonstration by solution decoupling

The presence of an oscillating dielectric disturbance breaks some of the previously established degeneracy by forcing the cosine solutions to occupy higher ϵ regions and the sine solutions to lower ϵ regions. This phase shifting between the two solutions is directly responsible for the opening of forbidden gaps. Applying perturbation theory under the constraint of small variation shows the bandgap as a function of mid-gap frequency to be $\Delta\omega/\omega\Delta/2$.²³ From this it follows that any periodic modulation of the dielectric function results in the formation of a forbidden gap while a small modulation results in a small gap and vice versa.

The formations of complete bandgaps in higher dimensions require more precise arrangements. Along each path taken there will be an opening of a forbidden gap predicted by the 1D argument. The formation of a global gap is accomplished by ensuring that all the 1D

gaps overlap in frequency and that each one is sufficiently large. Along these one-dimensional paths the mid-gap frequency, as it inversely relates to the periodicity $\sim c\pi/a (\epsilon)^{1/2}$, leads to the symmetry requirement of similar periodicities in all directions. Henceforth, the triangular lattice in two-dimensions and the face centered cubic lattice (FCC) in three-dimension possess the largest gaps. Examining how the fields behave at the boundaries reveals yet another criterion. At a dielectric boundary, whether the electric field is parallel or perpendicular, the energy density $\epsilon|E|^2$ will be discontinuous across the interface stemming from the boundary conditions that E_{\parallel} and ϵE_{\perp} are continuous. The discontinuity of the energy density gives rise to difficulties in confinement of the perpendicular electric field lines in the higher ϵ regions and the parallel field lines in lower ϵ regions. Factoring in this latter requirement, the designed structure should be composed of thin continuous channels running in all directions, facilitating strong confinement of lower bands and the forcing out of the higher bands, as these thin shapes cannot support multiple modes.¹⁸

The wave equation describing electromagnetic radiation in dielectrics is free of parameters constricting the solutions to specific length scales, under the assumption of macroscopic media, rendering the wave equations invariant of scale. This is a very useful property as difficult to manufacture structures at the optical lengths could be manufactured at larger, more easily attainable scales and the measured characteristics with some linear adjustments describe the structures at all length scales. This leads to simple relationships between electromagnetic problems that differ only by the linear scaling of distances and amplitudes. If the dielectric function is modified by linearly adjusting the spacing $\epsilon(r/p)$, where r represents the dielectric function's spatial dependence and p is the scaling factor, i.e. contraction

or expansion. After passing through the wave equations, the scaling adjusts the frequency eigensolutions by ω/p and the mode solutions by $H'(r') = H(r'/p)$. Or, if multiple solutions are desired for the same structure at different dielectric constants, linearly scaling the permittivity amplitude $\epsilon(r)/p$ and passing it through the wave equations shows that changing the amplitude of the dielectric contrast has no effect on the field distributions and it simply scales the frequency eigensolutions by $p^{1/2}\omega$.¹⁸

Another interesting property that does not require large dielectric contrasts, and for that matter even significant opening of forbidden regions, is the anomalous refraction observed at the interface of a photonic crystal with that of a homogenous medium. Under certain conditions, the refraction angle is found to be very sensitive to changes in the incidence angle and wavelength. This characteristic is attributed to the anisotropy of the bands and the dispersion that electromagnetic radiation could experience is theorized to be orders of magnitude greater than that observed in conventional prisms; hence, its appropriate naming convention, “superprism.” Since its introduction by Kosaka et al.,¹⁹ many have demonstrated this interesting property in two-dimensions and later in three-dimensions. Jesper Serbin and Min Gu recently demonstrated that superprism phenomena can take place in polymeric woodpile structures with an index contrast of 1.6 or lower, and a periodicity ratio of 2.8.²¹ The periodicity ratio is defined as the period of repetition of the structure in the stacking direction divided by the periodicity in the remaining directions. The strong dispersion characteristics of photonic crystals are thought to significantly advance wavelength division multiplexing technologies amongst others. Kosaka et al. have also demonstrated that photonic crystals can exhibit a lens like behavior found in conventional optics.²⁰ They have observed that self collimation amongst other lens like behavior

can take place in a three-dimensional photonic crystal, behaviors that typically arise from non linear effects (Kerr effect causing self focusing or soliton propagation) requiring high energy inputs and can very easily collapse. In photonic crystals, they are found to be independent of the light intensity and other requirements typically employed to prevent beam divergence or diffraction broadening.

2.2 MAXWELL'S EQUATIONS IN PERIODIC STRUCTURES

Photonic crystals, artificial structures designed primarily for the manipulation of electromagnetic fields, are naturally examined by the equations that describe these fields. Four equations, Gauss's law, Gauss's law for magnetism, Faraday's law of induction, and Ampere's law with Maxwell's correction govern all electromagnetic fields regardless of form and, therefore, encompass the fields in these structures.

$$\begin{aligned}\nabla \cdot E &= \frac{\rho}{\epsilon} \\ \nabla \cdot H &= 0 \\ \nabla \times E &= -\frac{\partial H}{\partial t} \\ \nabla \times H &= \mu J + \mu\epsilon \frac{\partial E}{\partial t}\end{aligned}\tag{1}$$

Gauss's law relates the electric charge contained within a closed surface to the surrounding electric field. Gauss's law for magnetism formulates that the total magnetic flux through a surface is zero; that is to say, that magnetic charges come in pairs dismissing the existence of magnetic monopoles. Faraday's law of induction coupled with Ampere's circuit law describes how a changing magnetic field is always accompanied by an electric field and vice versa.

Maxwell's addition of the displacement current to Ampere's law completed the theory by adding changing electric fields to the mix. Before Maxwell's addition, it was believed that magnetic fields are generated only by electric currents. The original form of the displacement current described a polarization current in a dielectric medium and led Maxwell to derive the wave equation by associating this displacement current to time-varying electric fields. A modern approach that replaces the original derivation and saves some cumbersome mathematics combines Ampere's circuit law with Faraday's law of induction. The derivation begins by the examination of Maxwell's equations in the Heaviside form with the following conditions. First, the medium is source free and lossless, that no current exists, and that $\epsilon(\mathbf{r})$ is real. Next, the medium is time-invariant such that any mode can be decomposed into a set of plane waves by Fourier theory. And finally, that the permeability inside the material is constant. Taking the curl of the two relations gives the following:

$$\begin{aligned}\nabla \times \nabla \times E &= -\frac{\partial \nabla \times H}{\partial t} = -\frac{\partial}{\partial t} \mu \epsilon \frac{\partial E}{\partial t} \\ \nabla \times \frac{1}{\epsilon} \nabla \times H &= \mu \frac{\partial \nabla \times E}{\partial t} = -\mu \frac{\partial}{\partial t} \frac{\partial H}{\partial t} \\ \frac{1}{c^2} &= \mu_0 \epsilon_0, \mu = \mu_0 \mu_r, \epsilon = \epsilon_0 \epsilon_r\end{aligned}$$

Using the cross product vector identity and the assumption that the fields are time-harmonic, the wave equations are obtained in the frequency domain.

$$\begin{aligned}\nabla \times \nabla \times E &= \left(\frac{\omega}{c}\right)^2 \mu_r \epsilon_r E \\ \nabla \times \frac{1}{\epsilon_r} \nabla \times H &= \left(\frac{\omega}{c}\right)^2 \mu_r H\end{aligned}\tag{2}$$

The wave equations in differential form provide a good starting point for any method chosen to solve a particular system. The two basic approaches in solving the wave equations in periodic media are the Finite Difference Time Domain Method (FDTD) and the Plane Wave Method (PWM). Both methods with some additional work can lead to the same results, but the FDTD is primarily used for finding the field distributions as a function of time within a structure whereas the PWM leads directly to the dispersion relation. Both heavily rely on dense computational data in obtaining high degrees of accuracy and, therefore, both are computationally intensive. Faster methods have been developed that can drastically reduce computation time and data storage requirements²² but the PWM is developed and implemented as a starting point. Either wave equation, whether it is a function of E or H, can be used to solve the system, but in practice the wave equation that is a function of H is preferred. The H field dependent wave equation is already in the form of a positive definite Hermitian Eigen system; however, with some additional work the E field dependent equation can be cast in that form as well. The depth of the complication in choosing the E field wave equation is reached when imposing the transversality constraint as it depends on the permittivity. If instead the electric displacement field is chosen, the dependence on the permittivity of the transversality constraint is eliminated, but then the permittivity appears three times in the wave equation and will undoubtedly complicate the computation, as it is now, is in the form of a generalized eigensystem. The H field dependent wave equation is already in a more pliable form and transversality constraint for the magnetic field is easily imposed. The H field inside the structure can be written in terms of a propagating function multiplied by a function with the same periodicity as the structure:

$$\begin{aligned}\bar{H}_{\bar{k}}(\bar{r}) &= e^{i\bar{k}\cdot\bar{r}} \cdot \bar{h}_{\bar{k}}(\bar{r}) \\ \bar{h}_{\bar{k}}(\bar{r}) &= \bar{h}_{\bar{k}}(\bar{r} + \bar{R})\end{aligned}$$

The periodic function h_k is Fourier expanded into the sum of plane waves and recombined to form

$$\begin{aligned}\bar{h}_{\bar{k}}(\bar{r}) &= \sum_{\bar{G}'} \bar{h}_{\bar{G}'}(\bar{r}) e^{i\bar{G}'\cdot\bar{r}} \\ \bar{H}_{\bar{k}}(\bar{r}) &= \sum_{\bar{G}'} \bar{h}_{\bar{G}'}(\bar{r}) e^{i(\bar{k}+\bar{G}')\cdot\bar{r}}\end{aligned}$$

Imposing the transversality constraint which essentially states that magnetic monopoles do not exist gives

$$\begin{aligned}\nabla \cdot \bar{H}_{\bar{k}}(\bar{r}) &= \nabla \cdot \sum_{\bar{G}'} \bar{h}_{\bar{G}'}(\bar{r}) e^{i(\bar{k}+\bar{G}')\cdot\bar{r}} = 0 \\ (\bar{k} + \bar{G}') \cdot \bar{h}_{\bar{G}'} &= 0\end{aligned}$$

The magnetic field is normal to the direction of propagation and leads directly to the separation of field components into their respective dimensions,

$$\begin{aligned}(\bar{k} + \bar{G}') &= |(\bar{k} + \bar{G}')| \hat{e}_3 \\ \hat{e}_1 \cdot \hat{e}_3 &= \hat{e}_2 \cdot \hat{e}_3 = 0\end{aligned}$$

where $(e_1, e_2, e_3,)$ are unit vectors and form an orthonormal triad allowing the decomposition of the magnetic fields into their directional components.

$$\bar{h}_{\bar{G}'} = \bar{h}_{1,\bar{G}'} \hat{e}_1 + \bar{h}_{2,\bar{G}'} \hat{e}_2 = \sum_{v=1,2} \bar{h}_{v\bar{G}'} \hat{e}_v$$

The decomposed magnetic field can now be introduced into the wave equation, *equation 2* by taking its curl.

$$\nabla \times \bar{H}_{\bar{k}}(\bar{r}) = i \sum_{\bar{G}'} \sum_{\nu} \bar{h}_{\nu \bar{G}'} [(\bar{k} + \bar{G}') \times \hat{e}_{\nu}] e^{i(\bar{k} + \bar{G}') \cdot \bar{r}}$$

and

$$\begin{aligned} \kappa(\bar{r}) \nabla \times \bar{H}_{\bar{k}}(\bar{r}) &= i \sum_{\bar{G}''} \sum_{\bar{G}'} \sum_{\nu} \bar{h}_{\nu \bar{G}'} \tilde{\kappa}_r(\bar{G}'') [(\bar{k} + \bar{G}') \times \hat{e}_{\nu}] e^{i(\bar{k} + \bar{G}' + \bar{G}'') \cdot \bar{r}} \\ &= i \sum_{\bar{G}} \sum_{\bar{G}'} \sum_{\nu} \bar{h}_{\nu \bar{G}'} \tilde{\kappa}_r(\bar{G} - \bar{G}') [(\bar{k} + \bar{G}') \times \hat{e}_{\nu}] e^{i(\bar{k} + \bar{G}') \cdot \bar{r}} \end{aligned}$$

Here, the Fourier expansion of the inverse of the permittivity is introduced,

$$\kappa(\bar{r}) = \frac{1}{\varepsilon(\bar{r})} = \sum_{\bar{G}''} \tilde{\kappa}(\bar{G}'') e^{i\bar{G}'' \cdot \bar{r}}$$

The variables \bar{G}' and \bar{G}'' are the variables of the expansions of the magnetic field and the permittivity and are reduced by equating $\bar{G} = \bar{G}' + \bar{G}''$. Taking the next curl, we get

$$\nabla \times [\kappa(\bar{r}) \nabla \times \bar{H}_{\bar{k}}(\bar{r})] = - \sum_{\bar{G}} \sum_{\bar{G}'} \sum_{\nu} \bar{h}_{\nu \bar{G}'} \tilde{\kappa}_r(\bar{G} - \bar{G}') \langle (\bar{k} + \bar{G}) \times [(\bar{k} + \bar{G}') \times \hat{e}_{\nu}] \rangle e^{i(\bar{k} + \bar{G}') \cdot \bar{r}}$$

Recombining the wave equation with the decomposed magnetic field and the applied curls, we get

$$- \sum_{\bar{G}} \sum_{\bar{G}'} \sum_{\nu} \bar{h}_{\nu \bar{G}'} \tilde{\kappa}_r(\bar{G} - \bar{G}') \langle (\bar{k} + \bar{G}) \times [(\bar{k} + \bar{G}') \times \hat{e}_{\nu}] \rangle e^{i(\bar{k} + \bar{G}') \cdot \bar{r}} = \left(\frac{w}{c}\right)^2 \mu_r \sum_{\bar{G}'} \sum_{\nu} h_{\nu \bar{G}'} e^{i(\bar{k} + \bar{G}') \cdot \bar{r}} \hat{e}_{\nu}$$

The wave equation can be pushed further by dividing out similar exponential factors, subtracting \bar{G}'' from the exponential factors on both sides, making use of the delta function identity by integrating over all space, and substituting \bar{G} for \bar{G}'' since it is a dummy variables.

$$\iiint_V d\bar{r}^3 e^{i(\bar{G} - \bar{G}'') \cdot \bar{r}} = \frac{1}{(2\pi)^3} \delta(\bar{G} - \bar{G}'')$$

By integrating over all space and by using the Dirac delta-function identity,

$$- \sum_{\bar{G}} \sum_{\bar{G}'} \sum_{\nu} \bar{h}_{\nu \bar{G}'} \tilde{\kappa}_r(\bar{G} - \bar{G}') \langle (\bar{k} + \bar{G}) \times [(\bar{k} + \bar{G}') \times \hat{e}_{\nu}] \rangle \frac{1}{(2\pi)^3} \delta(\bar{G} - \bar{G}'') = \left(\frac{w}{c}\right)^2 \mu_r \sum_{\bar{G}'} \sum_{\nu} h_{\nu \bar{G}'} \hat{e}_{\nu} \frac{1}{(2\pi)^3} \delta(\bar{G}' - \bar{G}'')$$

From above, substituting G for G'' and using the following identities,

$$\delta_{ij} = \begin{cases} 1 & i = j \\ 0 & i \neq j \end{cases}$$

$$\therefore \delta(G - G'')|_{G'' \rightarrow G} \equiv 1$$

and

$$\sum_{i=-\infty}^{\infty} a_i \delta_{ij} = a_j$$

the wave equation becomes

$$- \sum_{\bar{G}'} \sum_{\nu} h_{\nu \bar{G}'} \tilde{\kappa}_r (\bar{G} - \bar{G}') \langle (\bar{k} + \bar{G}) \times [(\bar{k} + \bar{G}') \times \hat{e}_{\nu}] \rangle = \left(\frac{w}{c}\right)^2 \mu_r \sum_{\nu''} h_{\nu'' \bar{G}} \hat{e}_{\nu''}$$

where, the equation is multiplied by $e_{\nu'}$ and is simplified by making use of the following vector identities

$$A \cdot (B \times C) = C \cdot (A \times B) = B \cdot (C \times A)$$

$$\langle (\bar{k} + \bar{G}) \times [(\bar{k} + \bar{G}') \times \hat{e}_{\nu}] \rangle \cdot \hat{e}_{\nu'} = - [(\bar{k} + \bar{G}') \times \hat{e}_{\nu}] \cdot [(\bar{k} + \bar{G}) \times \hat{e}_{\nu'}]$$

Applying the transformations, G to G'', G' to G and G'' to G', the relation will be in the form of^{23 (pg. 129)}

$$\sum_{\bar{G}} \sum_{\nu} [(\bar{k} + \bar{G}) \times \hat{e}_{\nu}] \cdot [(\bar{k} + \bar{G}') \times \hat{e}_{\nu'}] \tilde{\kappa}_r (\bar{G}' - \bar{G}) h_{\nu \bar{G}} = \left(\frac{w}{c}\right)^2 \mu_r h_{\nu' \bar{G}} \quad (3)$$

A more useful form of this relation from the perspective of computation is in matrix notation. The (k+G) terms can be rewritten in the form of vector magnitude multiplied by the direction unit vectors.

$$[(\bar{k} + \bar{G}) \times \hat{e}_{\nu}] \cdot [(\bar{k} + \bar{G}') \times \hat{e}_{\nu'}] = |(\bar{k} + \bar{G})| |(\bar{k} + \bar{G}')| [\hat{e}_3 \times \hat{e}_{\nu}] \cdot [\hat{e}_3 \times \hat{e}_{\nu'}]$$

$$[\hat{e}_3 \times \hat{e}_{\nu}] \cdot [\hat{e}_3 \times \hat{e}_{\nu'}] = \begin{pmatrix} \hat{e}_2 \cdot \hat{e}_2' & -\hat{e}_2 \cdot \hat{e}_1' \\ -\hat{e}_1 \cdot \hat{e}_2' & \hat{e}_1 \cdot \hat{e}_1' \end{pmatrix}$$

The relation written in Eigen value form,

$$\sum_{\nu\bar{G}} \psi^{\bar{k}}_{(\nu\bar{G}),(\nu\bar{G})'} h_{\nu\bar{G}} = \left(\frac{w}{c}\right)^2 \mu_r h_{(\nu\bar{G})'}$$

$$\psi^{\bar{k}}_{(\nu\bar{G}),(\nu\bar{G})'} = \tilde{\kappa}_r (\bar{G}' - \bar{G}) \cdot |(\bar{k} + \bar{G})| \cdot |(\bar{k} + \bar{G}')| \cdot \begin{pmatrix} \hat{e}_2 \cdot \hat{e}_2' & -\hat{e}_2 \cdot \hat{e}_1' \\ -\hat{e}_1 \cdot \hat{e}_2' & \hat{e}_1 \cdot \hat{e}_1' \end{pmatrix} \quad (4)$$

The relations arrived at are readily implemented by any computational tool such as Matlab and other vectorial computational aids. The variables k and G are found by closely examining the structure in reciprocal space where the k vectors are the directions chosen in the Brillouin zone and the G vectors are the reciprocal lattice vectors. An accurate representation of the inverse of the dielectric function κ is paramount and directly determines the accuracy of the results, but can be cumbersome to obtain.

2.2.1 Fourier expansion of the Permittivity

The difficulty in solving the eigenvalues for the eigensystem lies in obtaining an accurate representation of the primitive cell in the Fourier domain. Finding the analytical transform of the primitive cell will greatly reduce computation size and time, but an analytical transform is not necessary and sometimes even too difficult to obtain and in such cases one would have to rely on a Fast Fourier Transform (FFT) library and the problems that accompany them. Some of these are aliasing and considerably larger matrices that in turn require more storage space and computation time and results in problems with convergence.²⁴ Fourier theory dictates that any periodic signal can be reconstructed to its original form by the superposition of an infinite number of plane waves. In practice a reasonable degree of accuracy can be achieved with a

finite number of plane-waves. The dielectric function of the structure being itself periodic is rewritten as a sum of plane waves.

$$\varepsilon(\bar{G}r) = \frac{1}{\Omega} \int_{\Omega} \varepsilon(\bar{r}) e^{-i\bar{G}r} \partial r \quad (5)$$

where ε is the permittivity, $\bar{G}r$ is a Reciprocal lattice vector, and Ω is the volume of the elementary cell. The primitive cell contains two elliptical cylinders displaced and rotated about the origin and can overlap one another. The direct treatment of elliptical cylinders offset and rotated from and about the origin is cumbersome; therefore, utilizing the properties of the Fourier transform is ideal. The ellipticity, the offset, and the rotation are dealt with by the use of Fourier transform properties tabulated by Bracewell and are termed “affine transforms.”²⁵ Circular symmetry simplifies the form of the permittivity in the respective dimensions to a circular step function and in the remaining dimension the cylinders take the form of square waves.

$$\begin{aligned} \varepsilon_1(\bar{r}) = & \varepsilon_b + (\varepsilon_a - \varepsilon_b) \sum_{Rr} \prod (h - |y'' - \bar{R}z|) \prod (Rc - |p'' - p_1 - \bar{R}p|) \\ & + (\varepsilon_a - \varepsilon_b) \sum_{Rr} \prod (h - |y'' - \bar{R}z|) \prod (Rc - |p'' - p_2 - \bar{R}p|) \end{aligned} \quad (6)$$

here, the introduction of y'' and p'' is for the simplicity of illustration as they encompass the rotation and the ellipticity, and the displacement is shown by p_1 and p_2 . The two permittivity symbols, ε_a and ε_b represent the dielectric constants of the rods and the background respectively. The Π symbol is used to represent the step function, Rc is the radius of the rods, h is the length of the rods. In cases where the step function is a function of the radius, the step function is considered as a circ function. The translation vector Rp allows the permittivity function to span over the whole space.

To account for the possibility of overlap, in such a case when simple addition of the two cylinders produces erroneous results, an operation that merges the two cylinders while retaining

the original heights is developed. The union operation cannot be applied directly but conceptually, it describes the operation rather well. In cases where an overlap exists and cannot be avoided the mathematical equivalent of the union has to be applied and its development is presented in Appendix A.

To begin the Fourier treatment of the primitive cell, the equation of an ellipse is considered as a starting point. In calculus when dealing with the integration of an ellipse, it is common practice to perform a change of variables that pull out the ellipticity as a multiplicand and integrate over the remaining unit circle. A general equation for an ellipse is

$$\left(\frac{x}{a}\right)^2 + \left(\frac{z}{b}\right)^2 = 1 \quad (7)$$

where, “a” is the radius of the major axes, and “b” is the radius of the minor axes, changing the variables x and z to x’ and z’ gives,

$$x'^2 + z'^2 = 1$$

$$x' = \frac{x}{a}, z' = \frac{z}{b}$$

The standard way of finding the integration factor accompanying a change of variable is by the use of the Jacobian, defined as^{26 (pg. 974)}

$$\iint_R f(x, z) dA = \iint_S f(g(u, v), h(u, v)) \frac{\partial(x, z)}{\partial(u, v)} du dv$$

where

$$\frac{\partial(x, z)}{\partial(u, v)} = \begin{vmatrix} \frac{\partial x}{\partial u} & \frac{\partial x}{\partial v} \\ \frac{\partial z}{\partial u} & \frac{\partial z}{\partial v} \end{vmatrix} = \frac{\partial x}{\partial u} \frac{\partial z}{\partial v} - \frac{\partial z}{\partial u} \frac{\partial x}{\partial v} \quad (8)$$

For the transformation performed above to the ellipse, the integration factor is

$$\frac{\partial(x, z)}{\partial(x', z')} = \frac{\partial x}{\partial x'} \frac{\partial z}{\partial z'} - \frac{\partial z}{\partial x'} \frac{\partial x}{\partial z'} = (a)(b) - (0)(0) = ab$$

The equation of the Fourier transform of the permittivity has the exponential multiplicand that has real space and Fourier space dimension variables which must be transformed as well. Replacing x,y and z with their equivalents, collecting terms, and determining the transform of the Fourier space vectors, we arrive at

$$\begin{aligned}\bar{G}r \cdot \bar{r} &= Gx \cdot x + Gy \cdot y + Gz \cdot z \\ Gx \cdot x + Gy \cdot y + Gz \cdot z &= Gx \cdot ax' + Gy \cdot y' + Gz \cdot bz' \\ Gx' &= Gxa, Gy' = Gy, Gz' = Gzb \\ e^{-i\bar{G}r \cdot \bar{r}} &\Rightarrow e^{-i(Gx' \cdot x' + Gy' \cdot y' + Gz' \cdot z')} = e^{-i\bar{G}r' \cdot \bar{r}'}\end{aligned}$$

The variable change has reduced the complexity of integration due to ellipticity and now a variable change to reduce the complexity of rotation is developed. Because the cylinders are rotated about the z'-axis, only the variables representing the x'y'-plane will change, equivalent to performing a two-dimensional rotation. The standard system of equations that return the new variables after a two-dimensional counterclockwise rotation is²⁷,

$$\begin{bmatrix} x'' \\ y'' \end{bmatrix} = \begin{bmatrix} \cos(\beta) & \sin(\beta) \\ -\sin(\beta) & \cos(\beta) \end{bmatrix} \begin{bmatrix} x' \\ y' \end{bmatrix} \quad (9)$$

Applying the rotation transformation reduces the complexity of integration by aligning the coordinate axes with that of the cylinder. Substituting in the rotation equations and then solving for x' and y' necessitates solving the system of equations.

$$\left| \begin{array}{l} \sin(\beta) \cdot (x'' = \cos(\beta)x' + \sin(\beta)y') \\ \cos(\beta) \cdot (y'' = -\sin(\beta)x' + \cos(\beta)y') \end{array} \right|$$

$$\left| \begin{array}{l} (\sin(\beta) \cdot x'' = \sin(\beta) \cdot \cos(\beta)x' + \sin^2(\beta)y') \\ (\cos(\beta) \cdot y'' = -\cos(\beta) \cdot \sin(\beta)x' + \cos^2(\beta)y') \end{array} \right| +$$

$$\sin(\beta) \cdot x'' + \cos(\beta) \cdot y'' = 0 + y'(\cos^2(\beta) + \sin^2(\beta))$$

$$y' = \sin(\beta) \cdot x'' + \cos(\beta) \cdot y''$$

Following the same method one more time, the equation for x' is found.

$$\left| \begin{array}{l} \cos(\beta) \cdot (x'' = \cos(\beta)x' + \sin(\beta)y') \\ -\sin(\beta) \cdot (y'' = -\sin(\beta)x' + \cos(\beta)y') \end{array} \right|$$

$$\left| \begin{array}{l} (\cos(\beta) \cdot x'' = \cos^2(\beta)x' + \cos(\beta) \cdot \sin(\beta)y') \\ (-\sin(\beta) \cdot y'' = \sin^2(\beta)x' - \sin(\beta) \cdot \cos(\beta)y') \end{array} \right| +$$

$$\cos(\beta) \cdot x'' - \sin(\beta) \cdot y'' = x'(\cos^2(\beta) + \sin^2(\beta)) + 0$$

$$x' = \cos(\beta) \cdot x'' - \sin(\beta) \cdot y''$$

Any time a variable transformation is done the integration factor accompanying the said transformation needs to be found. Using the Jacobian, the integration factor is found to be

$$\frac{\partial(x', y')}{\partial(x'', y'')} = \frac{\partial x'}{\partial x''} \frac{\partial y'}{\partial y''} - \frac{\partial y'}{\partial x''} \frac{\partial x'}{\partial y''} = \cos(\beta) \cdot \cos(\beta) - \sin(\beta) \cdot \sin(\beta) = 1$$

As expected, the integration factor reduces to 1 since a rotation transformation will be absorbed by the bounds over which the function is integrated. As before, the variables in the exponential term need to be modified to complete the changes. Substituting for x' and y' with the newly found equivalents

$$Gx' \cdot x' + Gy' \cdot y' = Gx' \cos(\beta)x'' - Gx' \sin(\beta)y'' + Gy' \sin(\beta)x'' + Gy' \cos(\beta)y''$$

and by collecting terms and reassigning variables, we arrive at the transformed exponential term

$$\begin{aligned}
&= x''(Gx' \cos(\beta) + Gy' \sin(\beta)) + y''(-Gx' \sin(\beta) + Gy' \cos(\beta)) \\
Gx'' &= Gx' \cos(\beta) + Gy' \sin(\beta) \\
Gy'' &= -Gx' \sin(\beta) + Gy' \cos(\beta) \\
Gz'' &= Gz' \\
e^{-i\bar{G}r' \cdot \bar{r}'} &\Rightarrow e^{-i(Gx'' \cdot x'' + Gy'' \cdot y'' + Gz'' \cdot z'')} = e^{-i\bar{G}r'' \cdot \bar{r}''}
\end{aligned}$$

The necessary transformations that simplify otherwise complex mathematics have been established. This is allowed because the said transformations are linear and belong to a class of operations termed “affine transforms.” The resulting relations developed in Appendix A dealing with the overlap are now introduced. There, the permittivity function is written as an algebraic sum of its individual components, the two cylinders with a height of ϵ_a sitting in a background of ϵ_b . Substituting this permittivity function into permittivity integral and breaking up the integral, we get

$$\begin{aligned}
\varepsilon(\bar{G}r) &= \frac{1}{\Omega} \int_{\Omega} [\varepsilon_b + (\varepsilon_a - \varepsilon_b)(C_1 + C_2 - C_1 \times C_2)] e^{-i\bar{G}r \cdot \bar{r}} dr \\
&= \frac{1}{\Omega} \int_{\Omega} \varepsilon_b e^{-i\bar{G}r \cdot \bar{r}} dr + \frac{(\varepsilon_a - \varepsilon_b)}{\Omega} \left[\int_{\Omega} C_1 e^{-i\bar{G}r \cdot \bar{r}} dr + \int_{\Omega} C_2 e^{-i\bar{G}r \cdot \bar{r}} dr - \int_{\Omega} C_1 \times C_2 e^{-i\bar{G}r \cdot \bar{r}} dr \right]
\end{aligned}$$

Defining the integral of the product of C_1 and C_2 as the overlap integral, and using the Fourier transform duality, that multiplication in real-space is equivalent to convolution in the Fourier domain, the integral becomes

$$\begin{aligned}
I_{overlap} &= \frac{1}{\Omega} \int_{\Omega} C_1 \times C_2 e^{-i\bar{G}r \cdot \bar{r}} dr \\
&= \frac{1}{\Omega} \int_{\Omega} C_1 e^{-i\bar{G}r \cdot \bar{r}} dr * \frac{1}{\Omega} \int_{\Omega} C_2 e^{-i\bar{G}r \cdot \bar{r}} dr
\end{aligned}$$

Separating the rest of the integrals for ease of handling,

$$\begin{aligned}
I_1 &= \frac{1}{\Omega} \int_{\Omega} \varepsilon_b e^{-i\bar{G}r \cdot \bar{r}} dr \\
I_2 &= \frac{1}{\Omega} \int_{\Omega} C_1 e^{-i\bar{G}r \cdot \bar{r}} dr = \frac{1}{\Omega} \int_{\Omega} \sum_{Rz} \prod (h - |y'' - \bar{R}z|) \prod (Rc - |p'' - p_1 - \bar{R}p|) e^{-i\bar{G}r \cdot \bar{r}} dr \\
I_3 &= \frac{1}{\Omega} \int_{\Omega} C_2 e^{-i\bar{G}r \cdot \bar{r}} dr = \frac{1}{\Omega} \int_{\Omega} \sum_{Rr} \prod (h - |y'' - \bar{R}z|) \prod (Rc - |p'' - p_2 - \bar{R}p|) e^{-i\bar{G}r \cdot \bar{r}} dr
\end{aligned}$$

Since the first integral is simply the Fourier transform of a constant, it exists in the Fourier domain as a delta function, thus it will only influence the coefficients at the center of the spectrum, i.e., all reciprocal lattice vectors of zero length. And it simply evaluates to

$$I_1 = \frac{1}{\Omega} \int_{\Omega} \varepsilon_b e^{-i\bar{G}r \cdot \bar{r}} dr = \begin{cases} \varepsilon_b & \bar{G}r = 0 \\ 0 & \text{elsewhere} \end{cases}$$

The evaluation of the rest of the integrals requires a little more work. The summations in the integrals can be dropped since y'' and p'' span the whole domain and these coupled with the translation vectors Rz and Rp , span the whole space.

$$I_2 = \frac{ab}{\Omega} \int_{\Omega} \prod (h - |y'' - \bar{R}z|) \prod (Rc - |p'' - p_1 - \bar{R}p|) e^{-i\bar{G}r \cdot \bar{r}} dr''$$

The solutions can be decoupled into two regions when the reciprocal lattice vectors exist only at the origin and when they exist elsewhere. Considering the case of the origin when Gr is zero,

$$I_2 = \frac{ab}{\Omega} \int_{\Omega} \prod (h - |y'' - \bar{R}z|) \prod (Rc - |p'' - p_1 - \bar{R}p|) dr''$$

This integral evaluates to yielding the fractional volume of the cylinder with respect to the volume of the space it sits in,

$$I_2 = \frac{ab}{\Omega} \int_{-\frac{h}{2}}^{\frac{h}{2}} dy'' \int_0^{Rc} \int_0^{2\pi} p'' dp'' d\theta'' = \frac{abh\pi Rc^2}{\Omega}$$

Next, the case when the reciprocal lattice vector, Gr , is other than zero is examined. The step functions are removed from the integral as these are absorbed by the limits of integration.

$$\begin{aligned}
I_2 &= \frac{ab}{\Omega} e^{-i\bar{G}p'' \cdot p_1} \int_{-\infty}^{\infty} \prod (h - |y'' - \bar{R}z|) e^{-i\bar{G}y'' \cdot y''} dy'' \int_{-\infty}^{\infty} \prod (Rc - |p'' - p_1 - \bar{R}p|) e^{-i\bar{G}p'' \cdot p''} dp'' \\
&= \frac{ab}{\Omega} e^{-i\bar{G}p'' \cdot p_1} \int_{-\frac{h}{2}}^{\frac{h}{2}} e^{-i\bar{G}y'' \cdot y''} dy'' \int_0^{Rc} \int_0^{2\pi} p'' e^{-i\bar{G}p'' \cdot p''} dp''
\end{aligned}$$

The dot product in the exponential term is converted to spherical coordinates,

$$\begin{aligned}
e^{-i\bar{G}p'' \cdot p''} &= e^{-i(Gx'' \cdot x'' + Gz'' \cdot z'')} \\
x'' &= p'' \sin(\phi), \quad z'' = p'' \cos(\phi) \\
Gx'' &= Gp'' \sin(\theta), \quad Gz'' = Gp'' \cos(\theta)
\end{aligned}$$

Substituting for x'' and z'' and for Gx'' and Gz'' , we get

$$\begin{aligned}
(Gx'' \cdot x'' + Gz'' \cdot z'') &= Gp'' p'' \sin(\phi) \sin(\theta) + Gp'' p'' \cos(\phi) \cos(\theta) \\
&= Gp'' p'' [\sin(\phi) \sin(\theta) + \cos(\phi) \cos(\theta)]
\end{aligned}$$

and by making use of the product to some trigonometric identities, the reciprocal lattice vector G is rewritten as,

$$Gp'' \cdot p'' = Gp'' p'' \cos(\phi - \theta)$$

Making these substitutions in the integral, we arrive at

$$I_2 = \frac{ab}{\Omega} e^{-i\bar{G}p'' \cdot p_1} \int_{-\frac{h}{2}}^{\frac{h}{2}} e^{-i\bar{G}y'' \cdot y''} dy'' \int_0^{Rc} p'' dp'' \int_0^{2\pi} e^{-iGp'' p'' \cos(\phi - \theta)} d\phi$$

The following identities relate the area of a periodic exponential function in one period to a first order Bessel function, and allow simplifications in the integrals.

$$\frac{1}{2\pi} \int_0^{2\pi} e^{-iGp'p' \cos(\varphi-\theta)} d\varphi = J_0(Gp' p')$$

$$\int \phi J_0(\alpha\phi) d\phi = \frac{\phi}{\alpha} J_1(\alpha\phi)$$

These transformations allow I_2 to be rewritten and solved as

$$I_2 = \frac{2\pi ab}{\Omega} e^{-i\bar{G}p'' \cdot p_1} \int_{-\frac{h}{2}}^{\frac{h}{2}} e^{-i\bar{G}y'' \cdot y''} dy'' \int_0^{Rc} p'' J_0(Gp'' p'') dp''$$

$$= \frac{2\pi ab}{\Omega} e^{-i\bar{G}p'' \cdot p_1} \left[\frac{e^{-i\bar{G}y'' \cdot y''}}{-i\bar{G}y''} \right]_{-\frac{h}{2}}^{\frac{h}{2}} \cdot \left[\frac{p''}{Gp''} J_1(Gp'' p'') \right]_0^{Rc}$$

$$= \frac{2\pi abh}{\Omega} \cdot \text{sinc}\left(\bar{G}y'' \frac{h}{2}\right) \cdot \frac{Rc}{Gp''} J_1(Gp'' Rc) \cdot e^{-i\bar{G}p'' \cdot p_1}$$

The evaluation of integral I_3 is done much the same way as it was done for I_2 . The form of the equation is the same, and the only changes that actually occur are the values of the translation and rotation. The results obtained for the various integrals all have constants that are common between them and these are pulled together into a single descriptor, the fractional volume.

$$fr = \frac{abh\pi Rc^2}{\Omega}$$

At this point, the results can be cast in either form, the direct treatment of cylinders with overlap or by proceeding with an alternate elementary cell that provides the same results without having to consider overlap. The direct treatment that allows for overlap of the cylinders in the elementary cell reveals the permittivity function in Fourier space. Examining the solutions by considering the reciprocal lattice vectors at zero and at other than zero leads to the final form of the permittivity function. When the reciprocal lattice vectors are zero the permittivity does not depend on variables and its value defines the height of the spectrum at zero. Collecting all the results at zero gives

$$\begin{aligned}
\varepsilon(\overline{Gr}=0) &= I_1(0) + (\varepsilon_a - \varepsilon_b) \times (I_2(0) + I_3(0) - I_2(0) * I_3(0)) \\
&= \varepsilon_b + (\varepsilon_a - \varepsilon_b) [fr + fr - fr * fr] \\
\varepsilon(\overline{Gr}=0) &= \varepsilon_b + (\varepsilon_a - \varepsilon_b) [2fr - fr^2]
\end{aligned}$$

When the reciprocal lattice vectors acquire values other than zero, the permittivity in reciprocal space is defined by the product of a first order Bessel function with that of a Sinc function.

$$I_{2,3} = fr \cdot \text{Sinc}[Gy''(\beta_{1,2}) \frac{h}{2}] \cdot \frac{J_1[Gp''(\beta_{1,2})Rc] \cdot e^{-i\overline{Gp}''(\beta_{1,2}) \cdot p_{1,2}}}{Gp''(\beta_{1,2})Rc}$$

Recalling the transformations that were performed and substituting back to Gx, Gy, and Gz terms, the variables are

$$\begin{aligned}
Gy'' &= -Gx' \sin(\beta_{1,2}) + Gy' \cos(\beta_{1,2}) = -aGx \sin(\beta_{1,2}) + Gy \cos(\beta_{1,2}) \\
Gp'' &= \sqrt{Gx'^2 + Gz'^2} = \sqrt{(aGx \cos(\beta_{1,2}) + aGy \sin(\beta_{1,2}))^2 + (bGz)^2}
\end{aligned}$$

The numerical subscripts for the translation p and rotation β specify the cylinder that is considered within the primitive cell. The final form of the permittivity in Fourier space that combines the solutions in all the domains and allows the cylinders in the primitive cell to overlap, is

$$\varepsilon(\overline{Gr}) = \begin{cases} \varepsilon_b + (\varepsilon_a - \varepsilon_b)(2fr - fr^2) & \overline{Gr} = 0 \\ (\varepsilon_a - \varepsilon_b)(I_2 + I_3 - I_2 * I_3) & elsewhere \end{cases} \quad (10)$$

If an alternate primitive cell is found that does not contain overlaps of cylinders, then a relation describing that case can be formed by reducing the obtained results. The adjustment encompasses only the removal of overlap terms for all solutions. At Gr zero, the height of the spectrum at zero is reduced by removing the additional terms acquired by the overlap.

$$\begin{aligned}
\varepsilon(\overline{Gr}=0) &= I_1(0) + (\varepsilon_a - \varepsilon_b) \times (I_2(0) + I_3(0)) \\
&= \varepsilon_b + (\varepsilon_a - \varepsilon_b) [fr + fr] \\
\varepsilon(\overline{Gr}=0) &= \varepsilon_b + (\varepsilon_a - \varepsilon_b) 2fr
\end{aligned}$$

At reciprocal lattice vectors other than zero, the permittivity function is modified by removing the convolution term from the equation with overlap. The final form of the permittivity for the case of non-overlapping cylinders in the Fourier domain is

$$\varepsilon(\bar{G}r) = \begin{cases} \varepsilon_b + 2fr(\varepsilon_a - \varepsilon_b) & \bar{G}r = 0 \\ (\varepsilon_a - \varepsilon_b)(I_2 + I_3) & elsewhere \end{cases} \quad (11)$$

2.3 GENERATION OF THE INTERFERENCE PATTERN

The electromagnetic nature of light allows us to exploit its inherent periodicity to engineer a multitude of spatially periodic intensity distributions. These distributions can be converted into a special class of new material, photonic crystals, via holographic lithography. Manufacturing photonic crystals by the recording of designed interference patterns provides control over many degrees of freedom which can be manipulated to provide structures of different crystallographic classes. Holographic lithography involves the recording of formations of spatially periodic light intensity distributions from the interference of two or more coherent light beams. The electric field of a planar monochromatic light is mathematically described by

$$\bar{E}_m(\mathbf{r}, t) = \bar{E}_{o,m} e^{i \cdot (\bar{k}_m \cdot \bar{r}_m - \omega t + \phi_m)} \quad (12)$$

where m is the index of the beam, k is the wave vector, w is the angular frequency, the constant E_o is the electric field strength, and φ is the initial phase of the beam. The presence of multiple beams oriented such that they overlap in some region of space produce a new distribution, and this distribution is simply the vector sum of the individual components. The intensity in the region of overlap of the multiple beams is proportional to the square of the resultant vector sum.

The mathematical description shown is a general one and it applies to all types of polarization of monochromatic light whether linear, circular, or elliptical. Since the temporal component in the description freely propagates without any alterations, it falls out of the intensity equation due to the inner product with its complex conjugate.

$$\begin{aligned}
\bar{I}_1(\mathbf{r}) &= (\mathbf{E}_1 + \mathbf{E}_2 + \mathbf{E}_3) \cdot (\mathbf{E}_1^* + \mathbf{E}_2^* + \mathbf{E}_3^*) \\
&= \left(\dots + \bar{\mathbf{E}}_{o,m} e^{i \cdot (\bar{k}_m \cdot \bar{r}_m - \omega t + \phi_m)} + \dots \right) \cdot \left(\dots + \mathbf{E}_{o,n}^* e^{i \cdot (-\bar{k}_m \cdot \bar{r}_m + \omega t - \phi_m)} + \dots \right) \\
&= \left(\dots + \bar{\mathbf{E}}_{o,m} e^{i \cdot (\bar{k}_m \cdot \bar{r}_m + \phi_m)} + \dots \right) \cdot \left(\dots + \mathbf{E}_{o,n}^* e^{i \cdot (-\bar{k}_m \cdot \bar{r}_m - \phi_m)} + \dots \right) \\
&= \sum_m^N \sum_n^N \mathbf{E}_m \cdot \mathbf{E}_n^* e^{i \cdot (\bar{k}_m - \bar{k}_n) \cdot \bar{r} + \phi_m - \phi_n}
\end{aligned}$$

Here, N is the number of planar monochromatic beams of light that overlap and the other terms are as described before. For linearly polarized electromagnetic radiation, the intensity equation can be written in a simpler form²⁸

$$I(\mathbf{r}) = \sum_{m=1}^N E_i^2(\mathbf{r}) + \sum_{m < n}^N E_m \cdot E_n \cos[(k_m - k_n) \cdot \mathbf{r} + (\delta_m - \delta_n)] \quad (13)$$

And for the case where N is 2, the intensity equation simplifies to

$$I(\bar{r}) = E_{o1}^2 + E_{o2}^2 + 2E_{o1}E_{o2} \cos[\Delta\bar{k} \cdot \bar{r} + (\phi_1 - \phi_2)]$$

This is the equation for a one-dimensional intensity distribution or in other words, a one-dimensional grating with a spatial period of

$$|\Delta\bar{k}| = |\bar{k}_1 - \bar{k}_2|$$

As shown, the interference of two beams produces a one-dimensional periodic intensity variation whereas the interference of three and four beams produces two and three dimensional intensity variations respectively. Since one of the many principles of engineering is to generalize difficult scientific developments into easily reproducible and cost effective methods, the

generation of the intensity variation is produced with an off the shelf phase grating (Ibsen Photonics). The phase grating is designed such that it has a spatial period of 900nm and it diffracts into only three orders of substantial intensity, the 0th and the $\pm 1^{\text{st}}$ orders with an efficiency of 97.3%. Of this intensity 62% is diffracted to the 0th order and 35.3% to the $\pm 1^{\text{st}}$ orders. The electric fields of the three beams diffracted by the phase grating are mathematically described by

$$\begin{aligned}\overline{E}_1(\mathbf{r}, t) &= \overline{E}_{o,1} e^{i \cdot (\overline{k}_1 \cdot \overline{r}_1 - \omega t + \phi_1)} \\ \overline{E}_2(\mathbf{r}, t) &= \overline{E}_{o,2} e^{i \cdot (\overline{k}_2 \cdot \overline{r}_2 - \omega t + \phi_2)} \\ \overline{E}_3(\mathbf{r}, t) &= \overline{E}_{o,3} e^{i \cdot (\overline{k}_3 \cdot \overline{r}_3 - \omega t + \phi_3)}\end{aligned}$$

These three beams then interfere in the region they overlap to produce the periodic intensity distribution recorded by the photo resist. The region of overlap is determined by the cross sectional area of the impinging beam and the angle of diffraction. Since three beams produce a two-dimensional periodic intensity variation and the goal is to have a three-dimensional variation, the photo resist is subjected to two exposures. The second intensity variation is just a modification of the first such that the resultant structure exhibits a three-dimensional variation. There are two methods available that modify the second set of beams to achieve a three dimensional intensity variation. The initial phase components in the equations encompass this degree of freedom. Since the initial phase in holographic lithography is generally arbitrary and will only change the starting value, it can be ignored for the first exposure but it will become paramount for the second exposure. The phase components in the intensity equation of the second exposure can be controlled by either a physical displacement of the starting position or by placing a phase shifting plate in path of the beam. Either method produces the same result which is a phase difference between the first and second exposures. The total Intensity that the photo resist is subjected to is the sum of the two intensity distributions.

$$I_{total}(r) = \sum_{i=1}^6 E_i^2(r, t) + \sum_{\substack{i=1 \\ i < j}}^3 E_i \cdot E_j \cos[(k_i - k_j) \cdot r + (\delta_i - \delta_j)] + \sum_{\substack{i=4 \\ i < j}}^6 E_i \cdot E_j \cos[(k_i - k_j) \cdot r + (\delta_i - \delta_j)] \quad (14)$$

Written out into all of its components with the phase components replaced by displacements in the z direction, the relation becomes

$$\begin{aligned} I_{total}(\vec{r}) = & E_{o1}^2 + E_{o2}^2 + E_{o3}^2 + E_{o4}^2 + E_{o5}^2 + E_{o6}^2 \\ & + 2E_{o1}E_{o2} \cos[(k_1 \sin \phi_1 \cos \theta_1 - k_2 \sin \phi_2 \cos \theta_2) \cdot x + (k_1 \sin \phi_1 \sin \theta_1 - k_2 \sin \phi_2 \sin \theta_2) \cdot y + (k_1 \cos \phi_1 - k_2 \cos \phi_2) \cdot z] \\ & + 2E_{o1}E_{o3} \cos[(k_1 \sin \phi_1 \cos \theta_1 - k_3 \sin \phi_3 \cos \theta_3) \cdot x + (k_1 \sin \phi_1 \sin \theta_1 - k_3 \sin \phi_3 \sin \theta_3) \cdot y + (k_1 \cos \phi_1 - k_3 \cos \phi_3) \cdot z] \\ & + 2E_{o2}E_{o3} \cos[(k_2 \sin \phi_2 \cos \theta_2 - k_3 \sin \phi_3 \cos \theta_3) \cdot x + (k_2 \sin \phi_2 \sin \theta_2 - k_3 \sin \phi_3 \sin \theta_3) \cdot y + (k_2 \cos \phi_2 - k_3 \cos \phi_3) \cdot z] \\ & + 2E_{o4}E_{o5} \cos[(k_4 \sin \phi_4 \cos \theta_4 - k_5 \sin \phi_5 \cos \theta_5) \cdot x + (k_4 \sin \phi_4 \sin \theta_4 - k_5 \sin \phi_5 \sin \theta_5) \cdot y + (k_4 \cos \phi_4 - k_5 \cos \phi_5) \cdot (z - z_o)] \\ & + 2E_{o4}E_{o6} \cos[(k_4 \sin \phi_4 \cos \theta_4 - k_6 \sin \phi_6 \cos \theta_6) \cdot x + (k_4 \sin \phi_4 \sin \theta_4 - k_6 \sin \phi_6 \sin \theta_6) \cdot y + (k_4 \cos \phi_4 - k_6 \cos \phi_6) \cdot (z - z_o)] \\ & + 2E_{o5}E_{o6} \cos[(k_5 \sin \phi_5 \cos \theta_5 - k_6 \sin \phi_6 \cos \theta_6) \cdot x + (k_5 \sin \phi_5 \sin \theta_5 - k_6 \sin \phi_6 \sin \theta_6) \cdot y + (k_5 \cos \phi_5 - k_6 \cos \phi_6) \cdot (z - z_o)] \end{aligned}$$

A fixed wavelength laser impinging on the phase mask will emerge as three beams as depicted in the following diagram. Here, the axes are arbitrarily chosen and arranged such that the beam propagates in the positive z direction. The diagram depicts three k-vectors at some angle theta and phi in spherical coordinates. Theta is the angle of rotation of the beams while phi is the angle diffraction of the laser beam inside the photo resist.

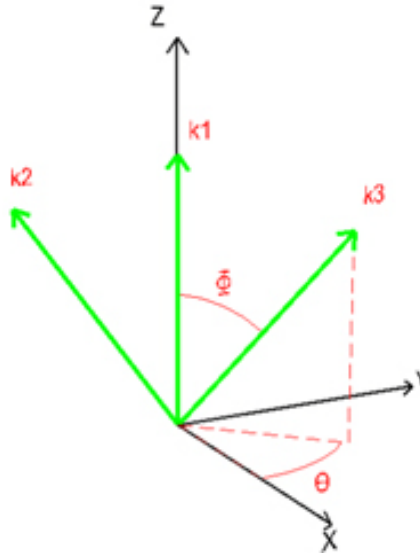


Figure 3. Orientation of k-vectors for light diffracted by the phase grating

The angle ϕ is not unique amongst the diffracted beams, the central beams possess one value of ϕ and the others possess another at normal incidence. As mentioned before, a phase grating is used to produce three in plane interfering beams at some angle ϕ . This angle is found by using Snell's law inside the photo resist and is found to be 19.8° when the wavelength of the laser is 514.5nm in free space and applies to all non-central beams. The three beams produced by the phase grating have two different electric field intensities; the central or undirected beam contains 62% and the two diffracted ones contain 35.3%. This is the same for the second exposure as well. Applying the aforementioned simplifications, a general formula that describes the intensity variation as a function of the angle of rotation, diffraction, and displacement is

$$\begin{aligned}
I_{total}(\bar{r}) &= 2E_{o1}^2 + 4E_{o2}^2 \\
&+ E_{o1}^2 \cos[k \sin \phi \cos \theta_1 \cdot x + k \sin \phi \sin \theta_1 \cdot y + (k - k \cos \phi) \cdot z] \\
&+ E_{o1}^2 \cos[-k \sin \phi \cos \theta_1 \cdot x - k \sin \phi \sin \theta_1 \cdot y + (k - k \cos \phi) \cdot z] \\
&+ \frac{1}{2} E_{o1}^2 \cos[-2k \sin \phi \cos \theta_1 \cdot x - 2k \sin \phi \sin \theta_1 \cdot y] \\
&+ E_{o1}^2 \cos[k \sin \phi \cos \theta_2 \cdot x + k \sin \phi \sin \theta_2 \cdot y + (k - k \cos \phi) \cdot (z - z_o)] \\
&+ E_{o1}^2 \cos[-k \sin \phi \cos \theta_2 \cdot x - k \sin \phi \sin \theta_2 \cdot y + (k - k \cos \phi) \cdot (z - z_o)] \\
&+ \frac{1}{2} E_{o1}^2 \cos[-2k \sin \phi \cos \theta_2 \cdot x - 2k \sin \phi \sin \theta_2 \cdot y]
\end{aligned}$$

Theta takes on two values, one being the angle of rotation of the first exposure, and the second being the angle of rotation of the second exposure. Phi takes on one value and is the angle of diffraction. As two rotation angles are demonstrated, two intensity equations are shown describing the respective intensity distributions. The specific intensity distribution for the orthogonal exposure is kept symmetric in the xy directions to mirror the orientation of the structure examined later.

$$\begin{aligned}
I_{90}(\bar{r}) &= 2E_{o1}^2 + 4E_{o2}^2 \\
&+ E_{o1}^2 \cos\left[\frac{\sqrt{2}}{2} k \sin \phi \cdot x + \frac{\sqrt{2}}{2} k \sin \phi \cdot y + (k - k \cos \phi) \cdot z\right] \\
&+ E_{o1}^2 \cos\left[-\frac{\sqrt{2}}{2} k \sin \phi \cdot x - \frac{\sqrt{2}}{2} k \sin \phi \cdot y + (k - k \cos \phi) \cdot z\right] \\
&+ \frac{1}{2} E_{o1}^2 \cos\left[-2 \frac{\sqrt{2}}{2} k \sin \phi \cdot x - 2 \frac{\sqrt{2}}{2} k \sin \phi \cdot y\right] \\
&+ E_{o1}^2 \cos\left[-\frac{\sqrt{2}}{2} k \sin \phi \cdot x + \frac{\sqrt{2}}{2} k \sin \phi \cdot y + (k - k \cos \phi) \cdot (z - z_o)\right] \\
&+ E_{o1}^2 \cos\left[\frac{\sqrt{2}}{2} k \sin \phi \cdot x - \frac{\sqrt{2}}{2} k \sin \phi \cdot y + (k - k \cos \phi) \cdot (z - z_o)\right] \\
&+ \frac{1}{2} E_{o1}^2 \cos\left[2 \frac{\sqrt{2}}{2} k \sin \phi \cdot x - 2 \frac{\sqrt{2}}{2} k \sin \phi \cdot y\right]
\end{aligned}$$

The intensity variation takes on a different form as the angle of rotation is varied. The second variation demonstrated is when the rotation angle theta takes on the value of 60° .

$$\begin{aligned}
I_{60}(\bar{r}) &= 2E_{o1}^2 + 4E_{o2}^2 \\
&+ E_{o1}^2 \cos\left[\frac{1}{2}k \sin \phi \cdot x + \frac{\sqrt{3}}{2}k \sin \phi \cdot y + (k - k \cos \phi) \cdot z\right] \\
&+ E_{o1}^2 \cos\left[-\frac{1}{2}k \sin \phi \cdot x - \frac{\sqrt{3}}{2}k \sin \phi \cdot y + (k - k \cos \phi) \cdot z\right] \\
&+ \frac{1}{2}E_{o1}^2 \cos\left[-2\frac{1}{2}k \sin \phi \cdot x - 2\frac{\sqrt{3}}{2}k \sin \phi \cdot y\right] \\
&+ E_{o1}^2 \cos\left[-\frac{1}{2}k \sin \phi \cdot x + \frac{\sqrt{3}}{2}k \sin \phi \cdot y + (k - k \cos \phi) \cdot (z - z_o)\right] \\
&+ E_{o1}^2 \cos\left[\frac{1}{2}k \sin \phi \cdot x - \frac{\sqrt{3}}{2}k \sin \phi \cdot y + (k - k \cos \phi) \cdot (z - z_o)\right] \\
&+ \frac{1}{2}E_{o1}^2 \cos\left[2\frac{1}{2}k \sin \phi \cdot x - 2\frac{\sqrt{3}}{2}k \sin \phi \cdot y\right]
\end{aligned}$$

2.3.1 Intensity Distribution Design

Since the intensity variations are then recorded by the photo resist, the phase delay forced on the second set of beams has to be such that the total intensity variation is both three-dimensional and well interconnected. The interconnectivity is a crucial aspect and it will determine whether the processed structure will support itself and remain crystalline. The interference of the first three beams produces a two-dimensional intensity variation in the form of elliptical cylinders arranged in a triangular array.

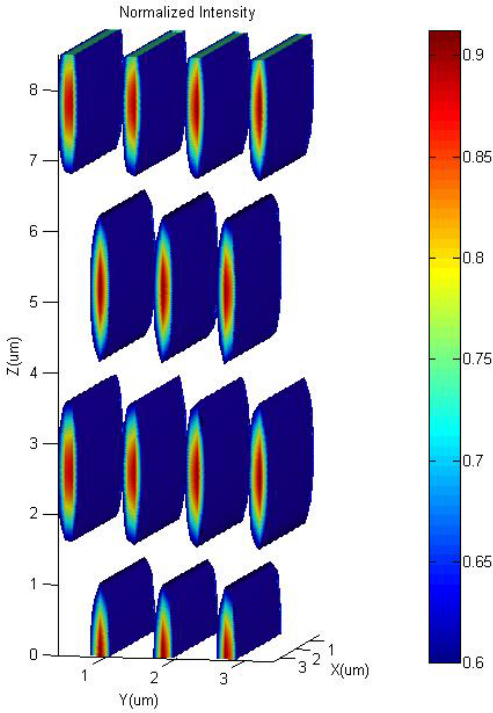


Figure 4. Normalized intensity distribution depicting the interference pattern generated by the phase grating

The diagram shows the equal energy contours of normalized intensity of 0.6 and above; however, energy is present in the entire region but it is of lower value than 0.6 and so for the purpose of illustration it is omitted. The energy of the background is an artifact of the interference and is contributed to mostly by the constant terms in the overall intensity equation. This background energy is an important topic that will be described later. Subsequent exposure places a second triangular array of cylindrical intensity variations displaced from the first by some distance z_0 such that the layers fully interconnect.

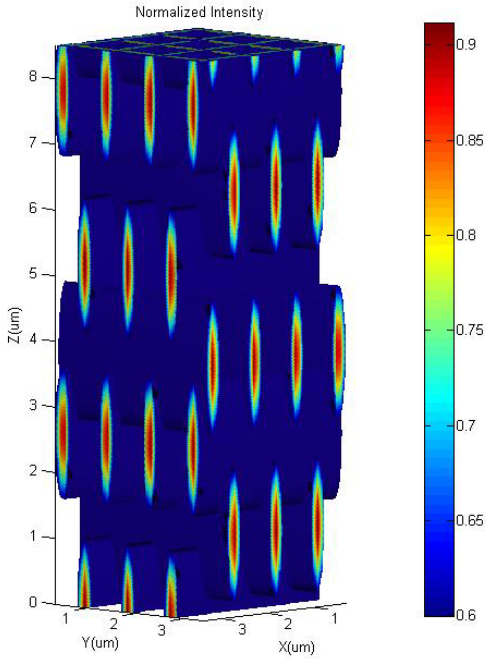


Figure 5. Normalized intensity distribution for two orthogonal exposures

The periodicity of the constructed intensity variation is determined by examining the simplified intensity equation of the two sets of beams. The periods of repetition are invariant of translation in the z-direction and they are found by setting the respective components to zero and taking the partial derivatives in the directions considered. For the case of orthogonal exposure, the periodicities of the structure in the x and y directions do not differ.

$$\begin{aligned}
\frac{\partial I_{90}}{\partial x} &= \frac{\partial \left[4E_{o1}^2 \cos\left(\frac{\sqrt{2}}{2} k \sin \phi \cdot x\right) + E_{o1}^2 \cos\left(2\frac{\sqrt{2}}{2} k \sin \phi \cdot x\right) \right]}{\partial x} \\
0 &= -4\frac{\sqrt{2}}{2} E_{o1}^2 k \sin \phi \sin\left(\frac{\sqrt{2}}{2} k \sin \phi \cdot x\right) \left[1 + \cos\left(\frac{\sqrt{2}}{2} k \sin \phi \cdot x\right) \right] \\
0 &= \left[1 + \cos\left(\frac{\sqrt{2}}{2} k \sin \phi \cdot x\right) \right] \\
\frac{\sqrt{2}}{2} k \sin \phi \cdot a_x &= \pi \\
a_{x,y} &= \frac{\pi}{\frac{\sqrt{2}}{2} k \sin \phi} = \frac{2\pi}{\sqrt{2} \frac{2\pi}{\lambda} \sin \phi} = \frac{1}{\sqrt{2} \frac{1}{\lambda} \sin \phi} = \frac{\lambda}{\sqrt{2} \sin \phi} \\
L &= \sqrt{a_x^2 + a_y^2} = \sqrt{2} \cdot a_{x,y}
\end{aligned} \tag{15}$$

The periodicity of the intensity variation in the z-direction is also invariant of translation and is found by taking the partial derivative in that direction while holding the x and y directions constant at any arbitrary value. The final form of the periodicity is shown as a function of wavelength and angle of diffraction inside the photo resist.

$$\begin{aligned}
\frac{\partial I_{60}}{\partial z} &= -4E_{o1}^2 (k - k \cos \phi) \sin((k - k \cos \phi) \cdot z) \\
a_z &= \frac{2\pi}{\frac{2\pi}{\lambda} (1 - \cos \phi)} \\
C = a_z &= \frac{\lambda}{1 - \cos \phi}
\end{aligned} \tag{16}$$

Following the same procedure one more time reveals the periodicity of the structure composed of intensity variations rotated by 60 degrees from one another. The invariance of the periodicity in the stacking direction to rotation is obvious as it is not a function of the angle of rotation.

$$\begin{aligned}
\frac{1}{2} k \sin \phi \cdot a_x &= \pi, \frac{\sqrt{3}}{2} k \sin \phi \cdot a_y = \pi, \\
a_x &= \frac{\lambda}{\sin \phi}, a_y = \frac{\lambda}{\sqrt{3} \sin \phi} \\
L &= \sqrt{a_x^2 + a_y^2} = 2\frac{\sqrt{3}}{3} \frac{\lambda}{\sin \phi}
\end{aligned} \tag{17}$$

The amount of phase shift forced on the second exposure by the translation of the origin determines whether the processed structure is well interconnected and is crystalline. The required translation in the z-direction to achieve a complete and symmetric interconnectivity is easily obtained by examining the overlapped intensity variations and is found to be a quarter of the periodicity in the z-direction.

$$z_0 = \frac{a_z}{4} = \frac{\lambda}{4[1 - \cos(\phi)]} \quad (18)$$

With this translation the layers of cylindrically confined energies will be interconnected with one another to form a three-dimensional variation in intensity which once processed will form the crystal template. Finally, an equation allowing the explorations of various contrast ratios as functions of the two angles is revealed.

$$\frac{C}{L} = \frac{\frac{\lambda}{1 - \cos \phi}}{\frac{\lambda}{\sin(\phi)\sin(\theta)}} = \frac{\sin(\phi)\sin(\theta)}{1 - \cos \phi} = \frac{\sin(\phi)\sin(\theta)}{2\sin^2\left(\frac{\phi}{2}\right)} \quad (19)$$

2.4 CRYSTALLOGRAPHIC ANALYSIS

The analysis of the periodic nature of the intensity variation is done through a well established set of tools in solid state physics. It is established that three-dimensional crystalline structures can vary between 7 crystal systems and 14 Bravais lattices.²⁹ It is important to know that how many of these 14 Bravais lattices the template can be cast into as some of the interference parameters are varied. This information will undoubtedly simplify any further analysis and presents one with a clearer view of the underlying properties of any structure. After careful

exploration, it is found that the structure of the template can be cast into a modified diamond structure with a two-atom basis. The diamond structure with a two atom basis is generally referred as the zincblende structure and is a part of the cubic crystal system and it is a face centered Bravais lattice (FCC). However, the template exhibits cubic symmetry only under certain conditions and therefore in the analysis, the periodicity in the stacking direction, z-direction, must be allowed to vary. For $C/L=2^{1/2}$ the lattice can be considered as an FCC primitive unit cell and at other ratios it is a face centered tetragonal (FCT) primitive unit cell. To cast the structure of the template into the zincblende form the structure in Cartesian coordinates is aligned such that the x and y axes are along the [110] and the [1-10] directions while the z coordinate axis remains unchanged.³⁰ This alignment is precise for an exposure rotation of 90° ; at others, the alignment has to be adjusted.

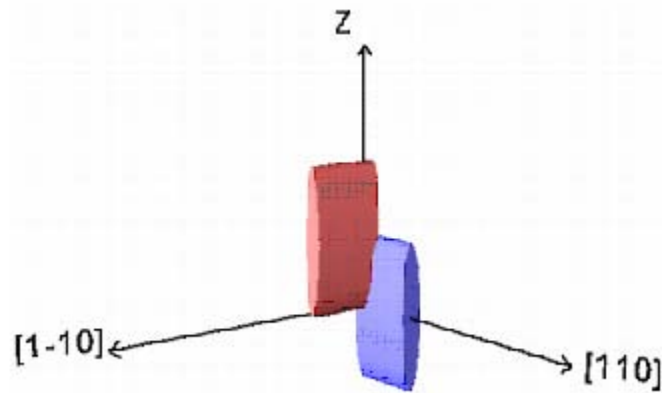


Figure 6. Diagram depicting the two atoms in the primitive cell along the respective orientations

With an orthogonal exposure, symmetric vectors that describe the structure are the FCC primitive vectors. The idea is to find a basic set of vectors that after integral repetition will reproduce the structure without any overlap or gaps.

$$\begin{aligned}
a_1 &= \frac{a_y}{2} \hat{y} + \frac{a_z}{2} \hat{z} \\
a_2 &= \frac{a_x}{2} \hat{x} + \frac{a_z}{2} \hat{z} \\
a_3 &= \frac{a_x}{2} \hat{x} + \frac{a_y}{2} \hat{y}
\end{aligned} \tag{20}$$

Computations in 3-dimensions over large areas are cumbersome with respect to time and storage requirements. It is paramount to reduce a primitive cell to a non-repeating region minimizing the extent over which calculations are performed. The continuation of the analysis in reciprocal space brings forth important features such as Bragg planes and a minimum non-repeating region in which computations are less cumbersome. The transformation of any periodic lattice to reciprocal space is accomplished by the following three primitive vectors that depend only on the real space lattice vectors.²⁹

$$\begin{aligned}
b_1 &= 2\pi \frac{a_2 \times a_3}{a_1 \cdot (a_2 \times a_3)} \\
b_2 &= 2\pi \frac{a_3 \times a_1}{a_1 \cdot (a_2 \times a_3)} \\
b_3 &= 2\pi \frac{a_1 \times a_2}{a_1 \cdot (a_2 \times a_3)}
\end{aligned} \tag{21}$$

This allows the conversion of the real space lattice vectors into reciprocal space, and these are

$$\begin{aligned}
b_1 &= 2\pi \left(-\frac{\hat{x}}{a_x} + \frac{\hat{y}}{a_y} + \frac{\hat{z}}{a_z} \right) \\
b_2 &= 2\pi \left(\frac{\hat{x}}{a_x} - \frac{\hat{y}}{a_y} + \frac{\hat{z}}{a_z} \right) \\
b_3 &= 2\pi \left(\frac{\hat{x}}{a_x} + \frac{\hat{y}}{a_y} - \frac{\hat{z}}{a_z} \right)
\end{aligned}$$

The k-space Wigner-Seitz primitive cell, also known as the first Brillouin zone, is the region in which a set of points exists that can be reached from the origin without crossing any Bragg planes. The first Brillouin zone can still be computationally large. Finding a set of points

within that truly minimize the volume of computation is done through symmetry operations that yield a region termed “the irreducible Brillouin zone.”¹⁸ The first Brillouin zone for an FCC crystal lattice is the body centered cubic Wigner-Seitz cell, but as the ratio of the periodicity varies, the geometry of the Wigner-Seitz cell also varies with this change.

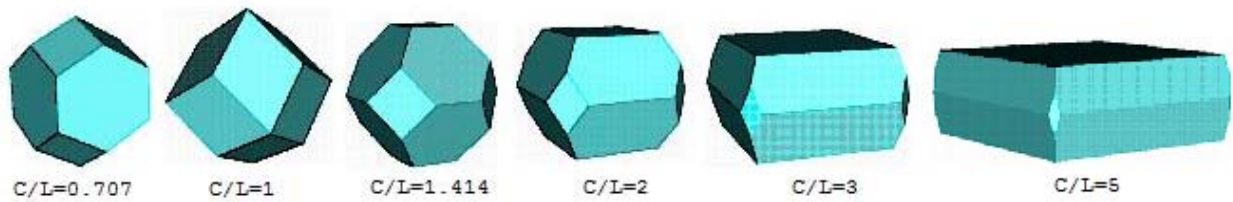


Figure 7. Evolution of the first Brillouin zone with changes in periodicity ratios

As the C/L ratio varies from .707 to 5 the geometry of the first Brillouin zone spans from a BCC and FCC hybrid to a highly distorted FCC, or an FCT Brillouin zone. With a $C/L=2^{1/2}$ ratio the first Brillouin zone acquires a full FCC symmetry.³⁰ Within the first Brillouin zone, a minimum region exists that is truly non-repeating and is found by examining the underlying symmetry of the primitive unit cell. The irreducible Brillouin zone for the case of full FCC symmetry is the volume region within the critical points.

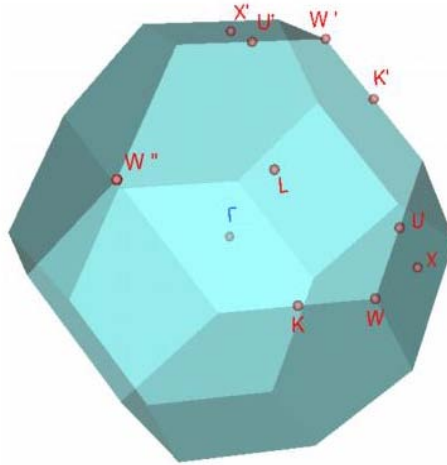


Figure 8. First Brillouin zone for a woodpile structure with $C/L=2^{1/2}$

For spherical atoms the unprimed critical points are sufficient to describe the irreducible Brillouin zone, but for the case of cylinders the additional points are required due to broken symmetry operations.

The second case explored is when the rotation of the second exposure is at a 60° angle to the first. In this case the symmetric set of primitive vectors is found by examining the structure and the vectors for orthogonal rotation in conjunction with the new primitive cell. Primitive vectors that correctly reproduce the 60° structure in real space and reciprocal space are

$$\begin{aligned}
 a_1 &= \frac{\sqrt{3}a_y}{2}\hat{y} + \frac{a_z}{2}\hat{z} & b_1 &= 2\pi\left(-\frac{1}{a_x}\hat{x} + \frac{1}{\sqrt{3}a_y}\hat{y} + \frac{1}{a_z}\hat{z}\right) \\
 a_2 &= \frac{a_x}{2}\hat{x} + \frac{a_z}{2}\hat{z} & b_2 &= 2\pi\left(\frac{1}{a_x}\hat{x} - \frac{1}{\sqrt{3}a_y}\hat{y} + \frac{1}{a_z}\hat{z}\right) \\
 a_3 &= \frac{a_x}{2}\hat{x} + \frac{\sqrt{3}a_y}{2}\hat{y} & b_3 &= 2\pi\left(\frac{1}{a_x}\hat{x} + \frac{1}{\sqrt{3}a_y}\hat{y} - \frac{1}{a_z}\hat{z}\right)
 \end{aligned}$$

The first Brillouin zone is found in much the same way as it was for the orthogonal exposure: the lattice points are examined in reciprocal space by identifying Bragg planes that form the

boundary of the structure. The symmetry of the Brillouin zone reflects the non-orthogonal exposure rotation seen in Figure 9 (right).

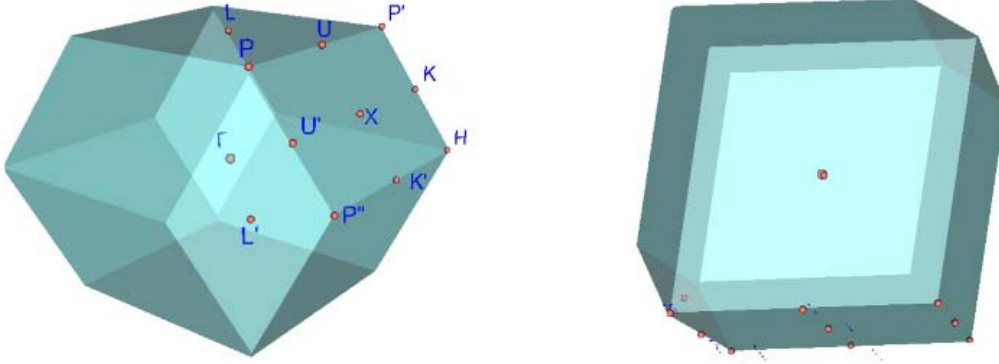


Figure 9. The first Brillouin zone for a 60° structure (left), with top view to show the respective angular distortion (right)

2.5 SOLVING THE WAVE EQUATION

The wave equation describing the interaction of electromagnetic radiation with that of periodic structures is derived and placed into vectorial form. The expression in such form simplifies the implementation into available computational aids, for example Matlab, for solving the eigenvalues of a system.

$$\sum_{\nu\bar{G}} \psi^{\bar{k}}_{(\nu\bar{G}),(\nu\bar{G})} h_{(\nu\bar{G})} = \left(\frac{w}{c}\right)^2 \mu_r h_{(\nu\bar{G})}$$

$$\psi^{\bar{k}}_{(\nu\bar{G}),(\nu\bar{G})} = \tilde{\kappa}_r (\bar{G}' - \bar{G}) \cdot |(\bar{k} + \bar{G})| \cdot |(\bar{k} + \bar{G}')| \cdot \begin{pmatrix} \hat{e}_2 \cdot \hat{e}_2 & -\hat{e}_2 \cdot \hat{e}_1 \\ -\hat{e}_1 \cdot \hat{e}_2 & \hat{e}_1 \cdot \hat{e}_1 \end{pmatrix}$$

Existing in the frequency domain, the equation depends on variables that describe the structure in reciprocal space. The variable k is a minimized set of reciprocal lattice vectors along the edges of the first Brillouin zone. The vector set, G , consists of integral combinations of the reciprocal lattice vectors describing the number and location of atoms in the vicinity of the origin.

$$\bar{G} = m_1 b_1 + m_2 b_2 + m_3 b_3 \quad (22)$$

The unit vectors e_i describe the two directions and are found by examining the directions of $(k+G)$. The permittivity of the structure encompassing all the geometric details is represented by κ in the relation. Having derived an analytical equation for the structure in the frequency domain, the arduous task of using a Fast Fourier Transform (FFT) library with its accompanying hurdles is avoided. The freedom of exposure rotation allows non-orthogonality in the primitive cell and as a consequence, finding an accurate Fourier representation by means of FFT would prove to be challenging. Along with the said difficulties that arise from non orthogonal systems, aliasing and other artifacts that pollute the results would accompany any FFT package. Although finding the analytical transform for a primitive cell could prove to be challenging as it was for the current structure, at the moment it is a preferable route in comparison to the alternative.

The relation describing the system is a Hermitian eigenvalue problem and can be implemented by numerical methods. Just as Fourier theory dictates, any periodic signal can be perfectly reconstructed by an infinite number of plane waves; however, in practice reasonable accuracy is achieved by a finite number of them. Since the problem exist in three-dimensions, considering only a small number of plane waves, n , along each direction explodes the problem into a $N=(2n+1)^3$ matrix. Needing only two dimensions, the three dimensional matrices are transformed into two-dimensional ones forming matrices of $2N \times 2N$ size. From these it follows that it is preferable to have a primitive cell composed of smoothly varying objects as they require

fewer plane waves to reproduce them with the same accuracy as would object with sharp edges. The primitive cell for the woodpile structure generated by the method employed in this thesis is elongated in the stacking direction yielding highly elliptical cylinders as atoms in the primitive cell. This anti-symmetry requiring higher frequency components for accurate reproduction in the Fourier domain demand more plane waves. The need for a high number of plane waves is also apparent upon examining the cylinders along their axes as in these dimensions they are represented by square waves. Improvements that replace discontinuous functions with smoothly varying ones by some sort of averaging are much needed as computations in the current form will fast become time-consuming for standard desktop computers.

Some properties of such systems described by wave equations simplify the implementation of components by considering only certain parts of the problem. The operator ψ is a linear that is if h_1 and h_2 are solutions, then h_1+h_2 are solutions. The operator is Hermitian, $(f, \psi g) = (\psi f, g)$. The dielectric function is positive definite yielding real eigenvalues.

The general scheme of implementation can be compounded into a few steps. First, the reciprocal lattice vectors are calculated from which the vector set G is found for a chosen number of plane waves. The three dimensional matrices describing position in the Frequency domain are then transformed into two-dimensional ones after which the permittivity matrix is solved. Next, the predetermined k -points along which calculations are performed are input and this set is further expanded by linear interpolation. Lastly, the unit vectors are found by examining the directions of $(k+G)$ in the respective dimensions. The eigenvalues are solved by Matlab's built-in function along with proper truncations. The large size of the matrices returns a vast number of

eigenvalues; however, only the lowest order modes are of importance and thus the returned eigenvalues are truncated to 10 modes. The Matlab program that solves for the dispersion relation is found in Appendix C.

The eigenvalues returned by the current implementation are validated with published works³⁰ and with MIT's Photonic Bands Package (MPB)²². The diamond structure composed of spherical atoms proved to be a viable test structure as the smoothly varying features facilitated small computations. Three hundred and forty three (343) plane waves returned indiscernible results from that found by MPB. However, the woodpile arrangement composed of cylindrical atoms poses computational difficulties on a Pentium 4 desktop computer with 2Gb of ram. To test the Matlab implementation, a symmetric woodpile arrangement is picked with a C/L of 1 and atomic radii of C/8 oriented orthogonally.

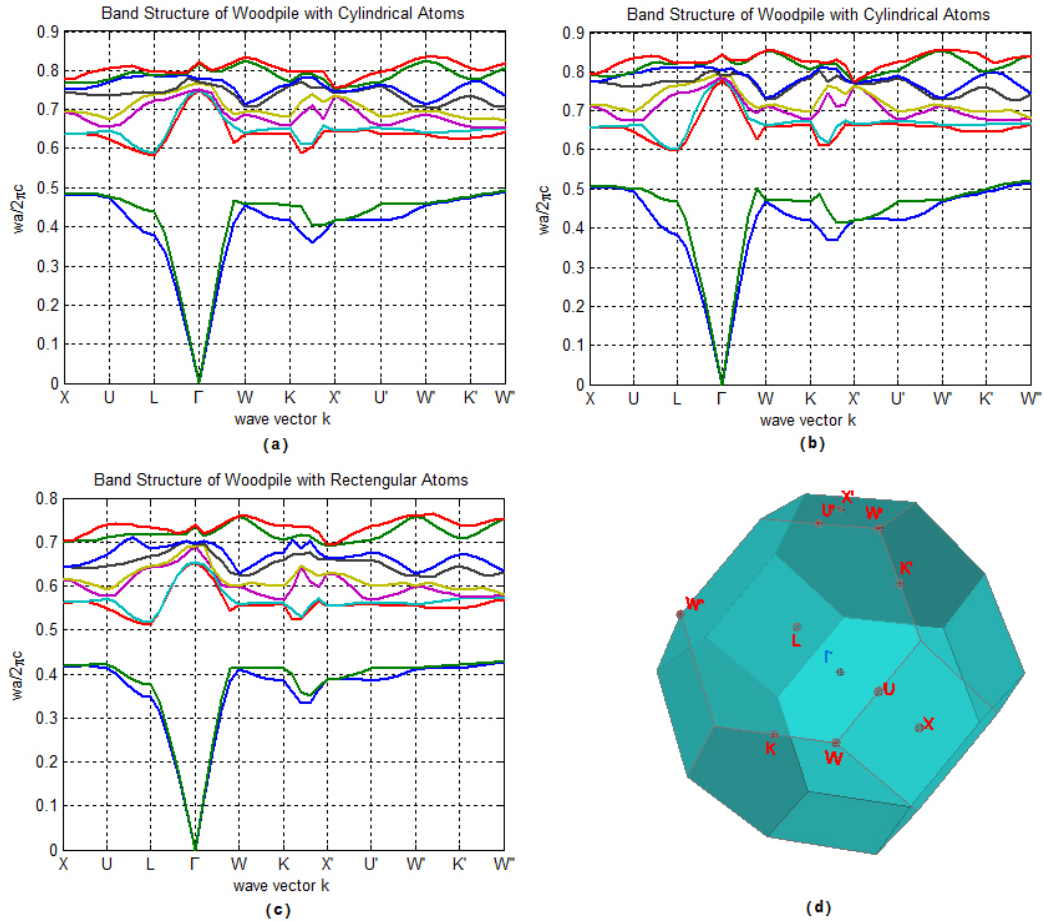


Figure 10. Band structures of a woodpile arrangement with $C/L=1$, radii = $C/8$. (a)-the band structure by Matlab with cylindrical atoms, (b)-by MPB with cylindrical atoms, (c)-by MPB with rectangular atoms, and (d)-First Brillouin zone with labeled k-vectors.

The plots of Figure 10 describe the dispersion relation along with the labeled k points in the first Brillouin zone. The Matlab implementation produced the band diagram (a) with 3375 plane waves reaching the limit of the said computer and consuming 8.3 hours for the computation. The direct implementation of the plane wave method with parallelized computing capable of handling very large computations will produce very accurate results, but its unavailability lead to the use of MPB to supplement and perform the many computations required to map out the system. While MPB is based on the plane wave method, it is implemented by making use of averaging methods to smooth out discontinuities in the dielectric

function and by using iterative eigensolvers in solving for the eigenvalues which in turn greatly reduce the computational resources needed. The band diagram (a) generated by Matlab has almost converged to the results obtained by MPB (b); the slight variations are the result of too few plane waves in the Fourier representation. The need to perform calculations at various C/L ratios led to the examination of using rectangular atoms as MPB does not have the capability to implement elliptical cylinders. The dispersion relations found by square atoms are similar to those found using cylindrical ones albeit an overall frequency offset. Using rectangular atoms will provide a good approximation for examining the size of the bandgap at various C/L ratios and especially at greater elongations. The periodicity ratio, C/L was defined as the ratio of the periodicity of the structure in the stacking direction to the magnitude of the periodicity along the other two directions. The sample MPB code that calculates the dispersions relation while maximizing the bandgap with respect to the lateral atomic dimension is found in Appendix D.

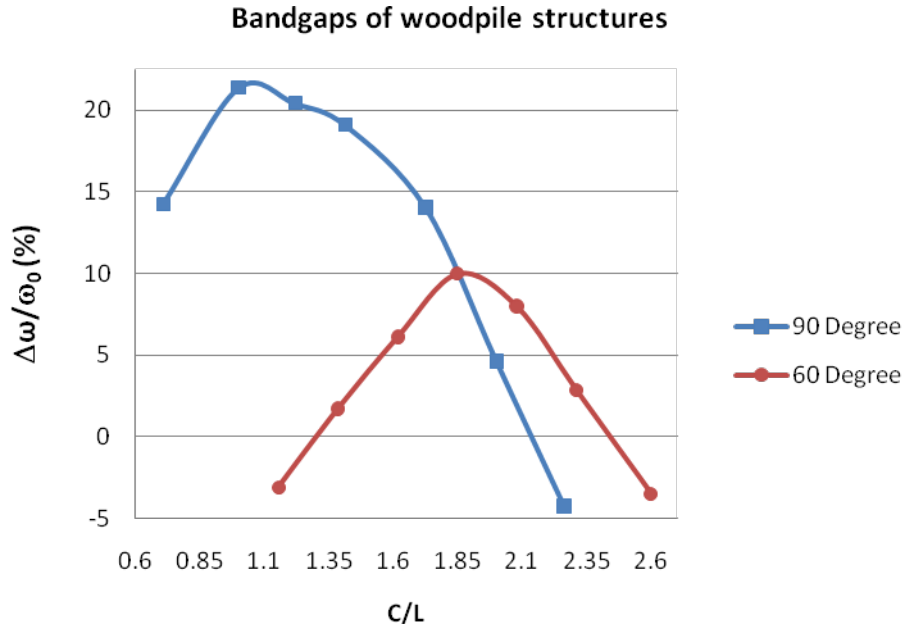


Figure 11. The variations in bandgap with changes in periodicity ratios for the two exposure rotations.

2.6 DRIVING CHEMISTRY

At the base of holographic lithography complex chemistry exists enabling the recording of designed intensity distributions to form durable structures withstanding the stresses of lithographic processing and of various inversion schemes. The commercially available SU-8 mixture (Microchem) consisting of a derivative resin with triaryl sulphonium salts as photoacid generators dissolved in organic solvents such as cyclopentanone is a suitable negative tone photo resist for the production of high resolution polymeric structures. SU-8, designed for the formation of multiplayer films with fine features, is used to provide films up to 2mm thick with a

contrast ratio of 20 or greater. Another requirement that SU-8 meets is that it is highly transparent in the near-UV and visible regions promoting uniform exposures throughout the film.

The intensity distribution is generated by a laser in the visible regime and since SU-8 is formulated to be sensitive to UV, it does not respond significantly to visible light; hence, some modifications are made. The additives that enable the recording of visible interference patterns are photosensitizers that absorb visible light and transfer the charges to the onium salts through the formation of charge transfer complexes. The photosensitizers used are 5,7-diiodo-3-butoxy-6-fluorone and phenyl-p-octyloxyphenyl-iodoniumhexafluoroantimonate (H-Nu 470 and OPPI from Spectra Group Limited, Inc.). Upon exposure to UV light, the photosensitizer transfers the acquired charges to the sulphonium salts generating photoacids in localized regions. The high temperature insensitivity of SU-8 plays a pivotal role in minimizing acid diffusion before post exposure bake and it prevents polymerization during exposure among other nonlinear changes.

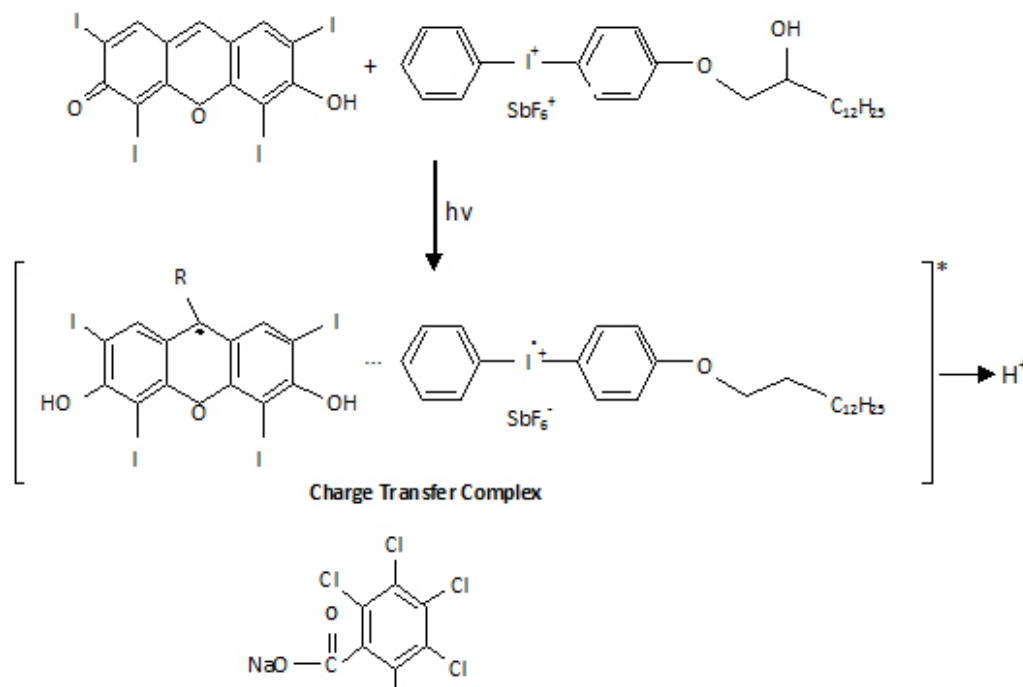


Figure 12. A general scheme for photosensitized cationic polymerization. Redrawn from Ref. ³³

Thermal excitation subsequent to exposure accelerates acid diffusion and induces cationic polymerization. The underexposed resist is then removed by propylene glycol methyl ether acetate (PGMEA from Microchem) followed by careful removal of solvents by isopropyl alcohol (IPA) and drying. The drying process is critical as structures with fine features can collapse from surface tensions between liquid and air interfaces and it is found that using IPA can greatly reduce what would otherwise be surface tensions if water is employed instead.

The DC term in the intensity distribution along with the lower energy oscillatory components complicates things as they also generate photoacids resulting in a non-zero acidic background that blurs the separation between exposed and underexposed regions. If not considered, this blurring will prevent the full opening of pores adding complications to subsequent stages of the process.

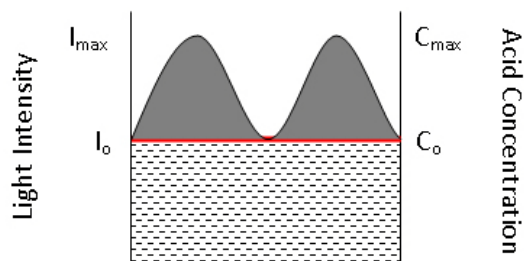


Figure 13. Diagram of the light intensity present in the region of interference with separated components into DC and oscillating terms. Redrawn from Ref. ³³

The non-zero background could be minimized by controlling some of the terms in the intensity equation, by optimizing the loading of the photosensitizer, or by chemical means. The distributions of photoacids determine the regions that polymerize and adding an acid scavenger reduces the concentration and minimizes acid diffusion. An appropriate amount of Triethylamine (TEA) which partially neutralizes the photoacids generated by the non-zero background is employed as a method of control over the effect of the background energy.³¹

3.0 EXPERIMENTAL PROCEDURES

3.1 EXPERIMENT SETUP

The generation of the interference pattern requires several components that are readily available. The laser beam is provided by an Argon Ion laser (Spectra-Physics Model 2020) adjusted for monochromatic output at 514.5nm. The output of the laser is linearly polarized and the accompanying electric field oscillates in the horizontal plane. Next, the propagating beam interacts with an electric shutter due to the small exit aperture of the shutter and it allows precise control over the exposure time down to 100ms. The active laser beam is then enlarged. This enlargement is necessary as it determines the length of the region over which the three-emerging beams overlap producing useful interference. The laser beam is enlarged by a biconvex two-lens system to a beam diameter of about a half an inch utilizing the available grating area.

The beam itself consists of several modes and the additional modes other than the TEM_{00} distort the interference pattern by reducing the contrast between the maximums and minimums in the oscillatory components as well as adding to the DC terms increasing the constant background energy. The removal of the additional modes is accomplished by a $1\mu\text{m}$ diameter spatial filter placed at the focal point of the magnification system. This particular size of the spatial filter is

calculated to be optimal at the wavelength of the laser, the incoming beam diameter, and the properties of the lens used to focus.

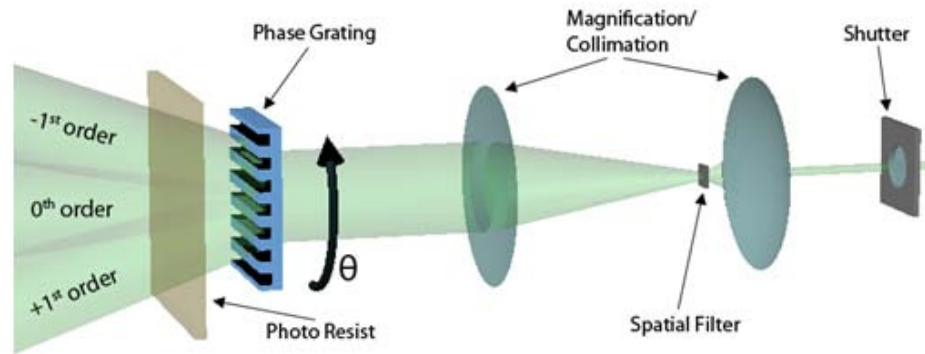


Figure 14. Experimental setup used to exposure samples to designed interference

Next, the magnified and collimated laser beam interacts with the phase grating diffracting it into three substantial orders. Originally, the phase grating was placed onto a rotation stage to allow rotation about the optic axis; however, this proved to be undesirable as it added unwanted displacements between the first and second exposures. To remove the undesirable degrees of freedom from the phase grating positioning, two phase gratings are fixed onto a polished quartz wafer at the chosen angle of rotation about the optic axes. The sample holder that positions the prepared photo resist parallel to the phase grating is mounted on a high precision motion stage (Newport PM500-4L) that allows displacement in the x y and z directions with $\pm 100\text{nm}$ precision. The interference setup in its entirety along with the Argon Ion laser is mounted on a vibration damping optical table and floated on air pockets through the exposure process. The power provided by the laser beam is measured to be 0.45W immediately before impinging on the phase grating.

The photo resist used to record the designed interference pattern is SU-8 2035, which is a high aspect ratio negative tone epoxy base polymer. Its maximum absorption is for ultraviolet light at 365nm and henceforth it is modified to extend its absorbance into the 515 nm range. SU-8 is modified by adding a photosensitizer to bring the interaction wavelength into the 515nm regime, a co-initiator acting as a catalyst, and propylene carbonate (PC) to assist in the dissolution. The photosensitizer is 5,7-diiodo-3-butoxy-6-fluorene (HNU-470) and has absorbance of 0.5 in the wavelength of interest. The co initiator, 4-octyloxyphenyl iodonium hexafluoro-antimonate (OPPI), assists in the charge transfer of the chemical reaction subsequent to exposure. A small amount of photo resist is prepared at a time, sufficient for about 10 days of trials due to the sensitivity of the mixture to thermal and electromagnetic radiation. The photo resist solution is composed of 40g of SU-8 2035, 0.5wt% of H-Nu-470 , 2.5wt% of OPPI, and 10ml of PC. The mixture is stirred for several hours to ensure complete dissolution that, in turn, results in higher contrast structures. Through experimentation, the difficulty of obtaining the desired result became transparent and is thought to be caused by the large background energy present in the interference pattern. To ease this hurdle, it is found that the addition of Triethylamine neutralizes some of the Lewis acids generated by exposure of the photo resist to radiation. The generation of Lewis acids is paramount as it allows the recording of the intensity pattern; however, the background energy present also generates these acids detrimental to the process by reducing the contrast between the exposed and underexposed regions.

The analysis of the samples is done by two types of imaging and a simple diffraction test. Once a sample is thoroughly dry it is examined by a high resolution optical microscope with a computer imaging interface. Examination by an optical microscope allows rough sorting of

samples into two categories: those that could possess the desired structural results and those that do not. The samples deemed for further analysis are then closely examined by a Scanning Electron Microscope (SEM) that is capable of resolving features in orders of magnitude greater than designed for this template. Finally, if one or two samples remain in the batch of dozens, they are subjected to diffraction tests that qualitatively reveal the disorder present on a larger scale. A clean diffraction image was the result of a large area defect minimum region. Other samples that had either very rough surfaces or small regions of structural integrity had diffraction images with low intensity peaks surrounded by surface scattered light spots.

The several variables that play a key role in the process, some intended and some not, each within its own frame of reference require a large number of iterations to achieve convergence. The intended set of variables are pre and post bake times, spin coating speed, the time length of exposure, the time length of developing, and the weight percent of TEA with respect to the amount of SU-8. Other variables detrimental to the process stem from the precision required to align the two sets of intensity distribution according to design criteria. The displacement of the phase grating by a motion stage rated at $\pm 100\text{nm}$ with $\pm 100\text{nm}$ uncertainty contributes a significant amount of error with respect to the required translation, specifically in the vicinity where the two intensity cylinders overlap as the error of the motion stage here is comparatively significant.

The alignment of the optical setup requires the most attention, as it is paramount that the translation of the second exposure takes place along the optic axes and having no quantitative method implemented to control this variable, it poses the greatest uncertainty. The pre and post

bakes adhere to established procedures developed by several groups;^{31,32} some variations were explored without any significant deviations. The variables of spin coating that determine the thickness and the uniformity of the SU-8 surface are held constant at providing a thickness of about 10 μ m. The thickness of the SU-8 mixture spun onto the substrate can, of course, vary throughout the process of fabrication due to the variable contents of TEA among others. Control over the variability of time length of developing is exerted by developing every sample for short time periods, and examining each one under low light conditions and repeating until exhaustion. The employment of these steps reduced the variables required for consideration to the time length of exposure, translation, and TEA concentration. The required translation is a known variable; however, displacements between the two gratings mounted on a quartz wafer could easily have unwanted offsets that coupled by the error of translation demanded attention. The two variables are explored by holding translation constant at an incremental value at which the exposure time is varied linearly in a predetermined range. The previous method is employed for each solution mixture of SU-8 containing various amounts of TEA from 1-40 mol%.

3.2 FABRICATION PROCEDURE

The process of producing the template can be split into three stages. In the first stage, the sample is prepared for exposure; next, the sample is exposed; and, third, the sample is post processed to reveal the designed template. In the sample preparation stage, the substrates are polished glass slides treated with piranha solution and dehumidified by baking on a hot plate. Each substrate is coated with a thin layer of OmniCoat (1 μ m) to enhance the adhesion of SU-8 to the substrate. The photo resist mixture is spun onto the treated substrates at speeds of 700 to 1500 rpm,

resulting in a range of thicknesses from 25 to 5 μ m. The prepared samples were then prebaked at 65 $^{\circ}$ C for about 30 min to remove the solvent from the photo resist mixture. The length of the prebake does not require precision as its goal is to remove the solvent and therefore it can be subject to alterations. Higher temperature prebake is not advised as it can act to generate Lewis acids and, in turn, reduce the contrast ratio before exposure to the desired radiation. The uniformity of the thermal radiation in the baking process and the gradual ramping of the temperature is however vital in the abatement of the inescapable surface effects.

The samples are then exposed to the designed interference pattern twice, once at one 0 degrees, and another at the angle of choice about the optic axes. Before exposure, the interference setup is realigned from a drift caused by vibration coupling and minute thermal variations. To demonstrate, two angles were primarily chosen for the second exposure, 90 $^{\circ}$ and 60 $^{\circ}$. The orthogonal exposure being fundamental in the design exhibits reduced crystal symmetry and in an attempt to correct for this, another exposure is demonstrated. The 60 $^{\circ}$ exposure rotation corrects for some of the destroyed symmetry resulting from elongation in the stacking direction. The duration of exposure is experimentally determined and is found to be optimal at 0.9s for both rotations. The exposed samples were then baked again for 10 minutes at 65 $^{\circ}$ C and for 5 minutes at 95 $^{\circ}$ C in order to crosslink the regions retaining significant amounts of Lewis acids. After cooling to room temperature, the samples were placed in the developing solution for 5 minutes and washed off with isopropyl alcohol and allowed to dry in air while maintaining a low intensity red light environment for the entire process.

4.0 EXPERIMENTAL RESULTS

4.1 STANDARD EVALUATION

Through experiment, a procedure was developed that adapted to the trial and error inherent in the process. The amount of SU-8 formulated was such that it provided enough samples that the iterations needed to produce convergence to a local optimum could be achieved in a window of about 10 days. This was roughly estimated to be about 100 samples out of which at least one sample that showed progress was obtained. After 10 days, a new solution was prepared as the additional uncertainty acquired by degradation of the solution to an already existing surplus was undesirable.

Initial experiments were conducted without the addition of an acid scavenger; instead, the amount of photo initiator was varied with partial success. After several iterations some of which provided excellent surface recordings, only few had openings and from this few only fractions had openings beyond the first layer. Initially a single phase mask mounted on a rotation stage was utilized adding additional uncertainty to the positioning of the second intensity distribution and henceforth increasing the number of trials needed to converge to somewhat acceptable results. The sample that reassured confidence as well as initiated the search for an alternative method of control over acid diffusion came after many trials with fully opened features only one layer deep.

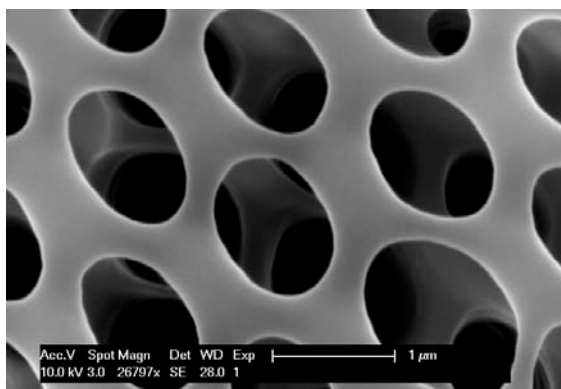


Figure 15. Surface SEM image of sample having 60° structure

A few iterations resulted in samples with very uniform openings but were confined purely to the surface. Imaging analysis with the depth in scrutiny showed that even after days of developing, the remaining unopened structure was not affected. This suggested that either the exposure time needed to be shortened or the background energy needed more careful attention.

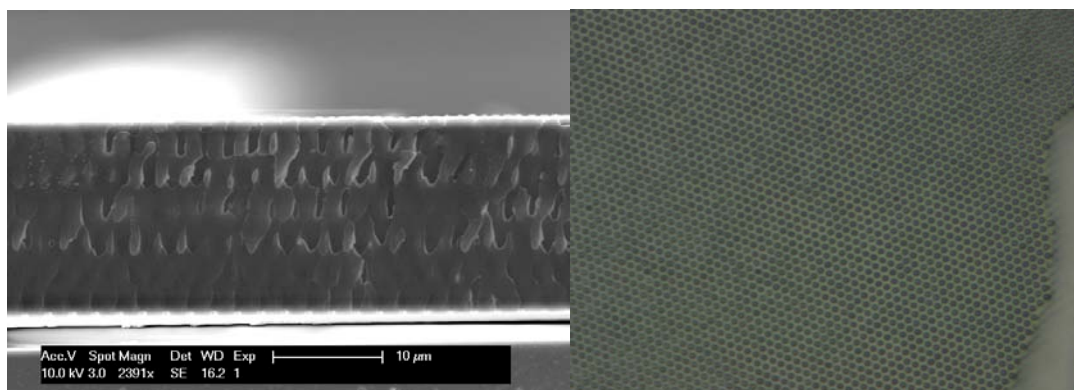


Figure 16. Sideview SEM image (left) showing partial opening, Surface optical microscope image (right) showing excellent surface structure

An alternative method of control over the background energy was accomplished by the addition of an acid scavenger, TEA. Various SU-8 solutions were made containing 1 to 40 mol% TEA each of the predetermined volume. Solutions that contained 30 to 40 mol% TEA provided structures with fully opened features of which only a few did not collapse pertaining to very short exposure and developing times. The precision that these solutions demanded in the exposure and developing stages resulted in thinner than expected features suggesting that the photo-acids were neutralized more than desired.

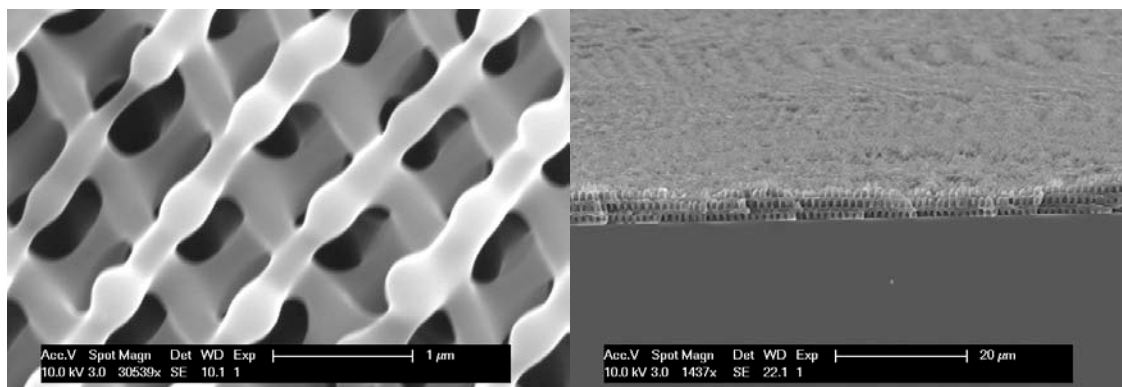


Figure 17. SEM image of 60° structure, left close examination of the surface, right examination of the side

A sample acquired by paying careful attention to the exposure and developing and furthermore to drying was obtained and full collapse was prevented. This structure exhibits structural integrity on a large scale; however, at examining the depth dimension, the partial collapse that took place is notable. This is seen as the sideways skewing of the image and it most likely took place in the drying process as it is here that the stresses exerted on the structure culminate from the capillary forces between the liquid and air interfaces.

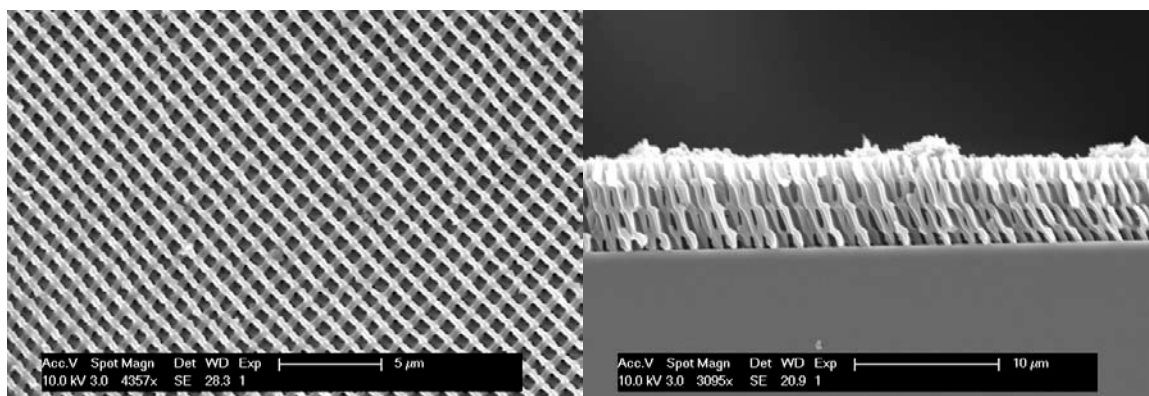


Figure 18. SEM image showing fully opened crystal with surface view (right) and side view (left)

The remaining solutions containing 1 to 20 w% TEA, 20% along with 0.9s exposure time yielded fully opened structures without any notable collapse. The SEM images that are magnified to reveal the structure contain insets pertaining to that which is predicted by simulation. The simulation is generated in Matlab by mapping out the overall intensity distributions and plotting the normalized isointensity volume of 0.5 and above. The Matlab program is found in Appendix B. The three-dimensional simulations are then rotated such that the crystal axes line up with that of the SEM images taken. This structure possesses a modified FCT symmetry and is the result of a 60° rotation between the first and second exposures.

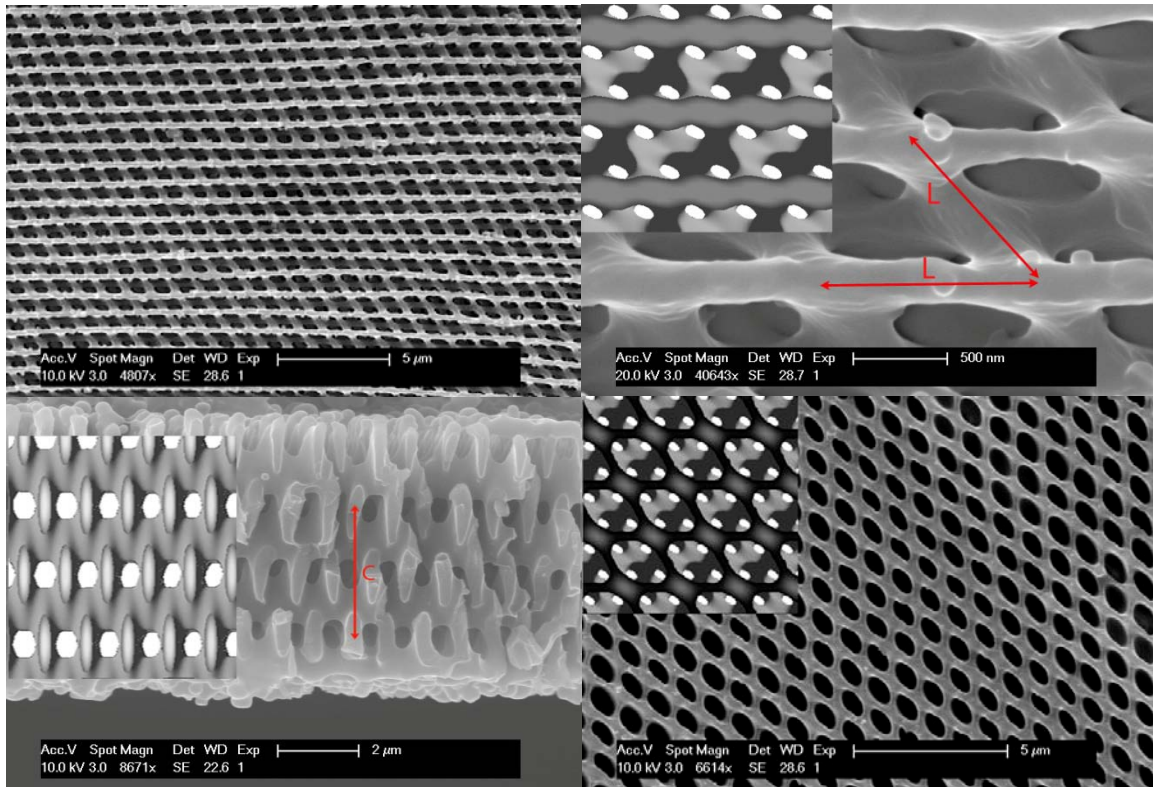


Figure 19. Surface image showing long range order (top left), closer view with predicted structure inset (top right), side view with prediction inset (bottom left), top view for another crystal plane (bottom right)

The periodicity of the template in the xy-directions is estimated by measurement tools built into the scanning electron microscope imaging system. In this direction, the lengths are equal in magnitude and the average of four measured values was $1\mu\text{m}$, whereas the estimated value was $1.05\mu\text{m}$. Performing the same measurements on the depth dimension gave the measured periodicity C to be anywhere from $3.8\text{-}5.5\mu\text{m}$ as opposed to the $5.2\mu\text{m}$ estimate. This measurement might not be as accurate as it is difficult to ascertain the rotation of the template. Prior hardships were encountered with the rotation of the sample holding stage to the exact vertical position.

4.2 DIFFRACTION ANALYSIS

The samples that were imaged and deemed to possess excellent surface features, or a fully opened structure with a rough surface, or a combination of both were then subjected to diffraction by a Helium Neon laser and a white light source. Although the implementation of the diffraction analysis did not reveal any quantitative results, it is however found to qualitatively assess whether the structures possessed global or local structural uniformity. Iterations prior to the addition of TEA provided samples that had very large areas of defect free regions limited to the surface. These of course had very clean diffraction images when subjected to a HeNe laser and a white light source.

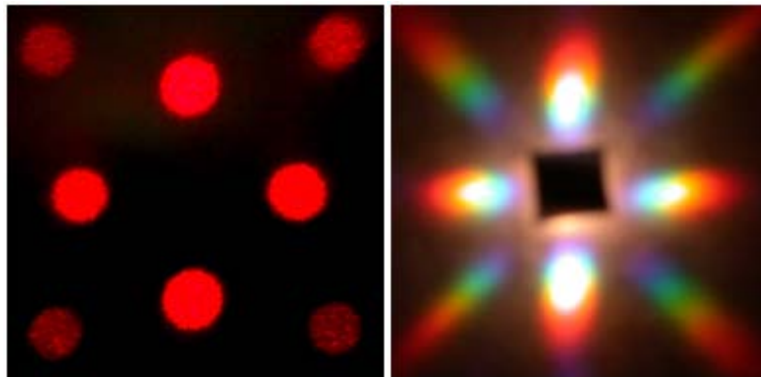


Figure 20. Diffraction image taken for 90° structure with a HeNe laser (left) and white light (right)

Iterations that provided samples with fully opened features in three-dimensions generally had a rough surface from collapse as thin protruding membranes did not have any lateral support to withstand the forces of surface tension. The diffraction images from these samples were polluted with light spots as the random surface scattered some of the rays off axes.

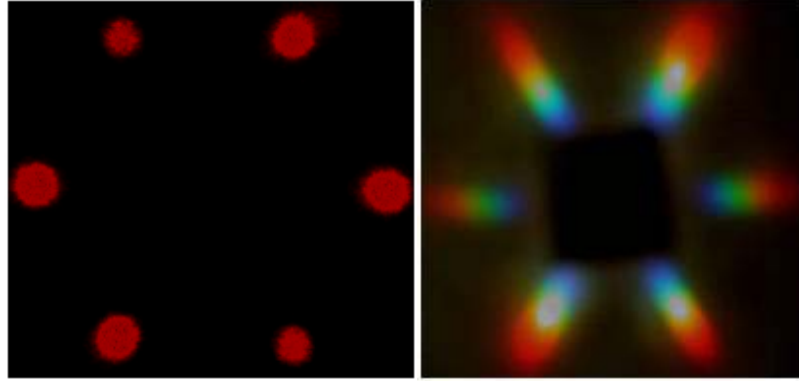


Figure 21. Diffraction image taken for 60° structure with a HeNe laser (left) and white light (right)

A sample processed with the solution mixture containing 20 mol% TEA with an exposure time of 0.9s proved to have the greatest chance of providing samples that had both fully opened features throughout the structure along with clean surface features if the developing and drying were controlled very carefully. Careful developing was done through continuous immersion into the two petri dishes placed side by side, one containing the SU-8 developer, the other the isopropyl alcohol. This allowed the removal of washed away components that could potentially adhere to the surface of the sample.

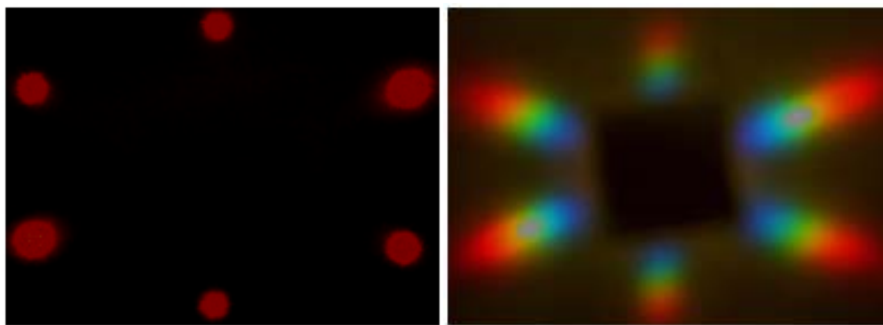


Figure 22. Diffraction image taken for 45° structure with a HeNe laser (left) and white light (right)

5.0 ANALYSIS

5.1 SUMMARY

This experiment was done under the guidance of Dr. Yuankun Lin, in collaboration with the University of Texas-Pan American. He provided a recipe for the SU-8 mixture along with background information necessary to fabricate the structure including some preliminary band diagrams. The recipe for the SU-8 mixture was later altered by varying the photo initiator and co-initiator in an attempt to counteract the effects of the background energy and later these detrimental effects were mitigated by the addition of TEA. The mathematics driving the process including the simulated predictions of the band diagrams was developed post experiment due to the needed expertise in solid state physics. With the acquisition of expertise in solid state physics and electromagnetic theory, the driving mathematics was established based on the need to place the experiment in proper context. The mathematics developed post experiment led to the discovery of the lack of significant global openings beyond a periodicity ratio, C/L of 2.35. The predicted C/L ratios for the structures fabricated are 5.7 and 5 for 90° and 60° exposure rotations respectively. The periodicity of the structure in all dimensions is strongly dependent on two components: namely, the phase grating and the laser. The particular components employed were those on hand at the time.

The analysis of the structure in the frequency domain was not without some difficulties. The solution of the Eigen system by Plane Wave decomposition is fairly straight forward albeit the placement of the wave equation in a simplified computational form was not without tedious mathematics. The true depth of mathematics was reached once the equations called for an adequate Fourier representation. Fortunately, the treatment of various multidimensional shapes in Fourier space along with their linear transformation has been previously documented. Although, the derivation of the Fourier representation of the primitive cell was nearing completion at the time of discovery of the text containing pertinent information,²⁵ it was reassuring to be able to compare it to previously established mathematics. The implementation of the Plane Wave Method (PWM) was done in Matlab in vectorial form through the use of its packages optimized for large computations. The PWM is a robust method capable of providing very accurate predictions as long as vast amounts of computational resources are available. Solving this system on a 3GHz Pentium 4 processor with 2GB of RAM did prove to be difficult, the largest computation possible on this system was with 3375 Plane Waves (PW) consuming 8.3 hours. Structures with elongation, such as the case in this experiment, possessing reduced symmetry required even more PW for the band diagram to converge necessitating the use of MPB. MPB has built-in functions to provide various shapes in three-dimensions but not an elliptical cylinder; therefore, a rectangular slab is used to approximate the shape of the atoms. This approximation is deemed adequate as it has been shown that the band diagram of the system does not significantly change with the change of atomic shape. The variations in the size of the bandgap are not significant. The use of MPB in predicting the band diagrams lead to a partial bandgap map of the system summarized by the plot that relates the size of the bandgap to the structure elongation factor, i.e. periodicity ratio C/L of the two exposure rotations.

As a measure of success in predicting the structure of the template, the geometric properties were compared. The structure to the naked eye strongly resembles that which is simulated, but with the help of built-in tools of the Scanning Electron Microscope rough measurements were done to compare to simulations. From the measured quantities, the largest deviation is found in the periodicity of the stacking direction C as its measured value was ranged from 3.8-5.5 μm . The large deviations in the measured values of C could come from the alignment issues of the sample holding stage within the SEM or a bad estimate of the index of refraction of the photo resist solution, the prior is likely. At examining the simulation of the isointensity surface, an isointensity value of 0.5 adheres to the template the closest though a more analytical approach is preferable. At the moment one does not exist.

During the analysis of the variables deemed to provide control over the fabrication of the structure, no systemic regularities were observed in the displacement. Bringing the second phase grating into play by displacing the motion stage in the lateral direction coupled with that along the optic axis made it difficult to hone in on a subset of values in displacement. If the experiment consisted of one phase grating, the uncertainty in translation along the optic axis would have been manageable. As no quantitative method of control over this variable was implemented, translation to the second phase grating randomized the system. The optimal values for the two controllable variables of fabrication were found with ease: the exposure time found to yield the best structure was 0.9 seconds for 20 mol% TEA solutions. An attempt was made to counteract the elongation by generating structures by other than orthogonal secondary exposure. Although, the demonstrated 60° rotation did have a reduced periodicity ratio, it was not reduced

enough for the structure to possess a global forbidden band. In the simulation, as the rotation angle decreases from normal, the peak of the size of the gap shifts to higher C/L ratios, but the maximum obtainable gap is also reduced. There could still be a rotation angle for which a global forbidden region exists; however, this was not explored.

The manufacture of photonic crystal templates by means of holographic lithography returned mixed results. This method of crystal fabrication using SU-8 as a medium is proven to be viable at providing the structures designed for. The geometric properties of the structure obtained by experiment adhere closely to that obtained by simulation with the largest deviation being in that of the periodicity C ; more analysis is needed to uncover the source. SU-8, formulated for interaction with radiation in the UV regime was successfully modified to interact with visible light by the action of charge transference. Overall, the manufacture of crystal templates by the use of holographic lithography was successful and the difficulties that were encountered are those of error in design.

The use of two one-dimensional phase gratings necessitated physical displacements that by their nature add a great deal of uncertainty to the process. Relying on devices to add displacements comparable in magnitude to the wavelength in the visible regime should generally be avoided. In cases where the design calls for these types of mechanisms, reevaluation should take place as the uncertainty acquired calls for a great deal of trial and error. The initial goal being the manufacture of crystal templates that by means of inversion would provide a structure possessing a global forbidden region was not met and is a direct result of the order of procession. The bandgap analysis of the predicted structure should have taken place prior to experiment as in that case, the results of simulation would have necessitated reevaluation in design. However, all

is not lost as the structure fabricated has potential uses even without possessing global openings such as the strong dispersion effects demonstrated for structures of this type towards the enhancement of wavelength division multiplexing. And, as the groundwork having been laid out, the manufacture of an alternate design will without a doubt be expedited.

5.2 FUTURE WORK

Every stage of the experiment from simulation to fabrication could be subjected to in-depth evaluation and, as a result, implementable methods that provide improvements would surface. The large computations required to accurately predict the band structure could be greatly reduced by employing averaging in the treatment of the plane wave decomposition of the “atoms” along with iterative methods in obtaining the solutions to the Eigen system. The uses of these improvements have been demonstrated by Steven Johnson et al., as their program, MPB, solves complex systems with a fraction of the resources that the direct implementation calls for. The code relying on analytical representations of the structure in the frequency domain could be improved by developing a method that accurately determines the same representation by means of FFT as finding the analytical transform could prove to be arduous for non-symmetric atomic shapes possessing complex geometries.

Prior to the addition of TEA which partially neutralized the generated photo acids and in turn mitigated the effects of the background energy, samples were acquired that possessed excellent surface recordings. Despite the fact that these had very clean diffraction images, they were categorized as partial successes at the time. At examination of the process with the

positioning in focus, these mistakes were thought to provide a much needed solution alleviating the need for displacement. The problems that stem from the use of one-dimensional phase gratings are the result of the need for translation for the formation of three-dimensional structures. On the other hand, if a multi-dimensional grating is used, this need for translation could be eliminated. The design and manufacture of a grating that generates a desired intensity distribution that removes one or all required physical displacements would make the process of holographic fabrication of crystal templates highly repeatable. Furthermore, since true FCC lattices are the ones that possess the largest gaps, whether in the form of single or multi atomic primitive cells, further exploration could reveal the possibility of generating interference patterns that come closer and closer to these parent structures.

Even though the experiment was met with partial success, the work in the current frame of reference is not complete. With some additional work, a complete characterization of the system could be obtained that explored the possibility of forbidden regions at secondary exposure rotation angles much lower than demonstrated. The characteristic plots that relate the size of the band gaps to C/L ratios could be expanded by the addition of other rotation angles to discover an angle that could be manufactured with the current setup yielding a global opening in the gap, although the gap might be small. An addendum to the process that provided a measured band diagram of the system to compare to simulated ones would complete the work within the current frame. Although, measuring the bandgap would most likely require the conversion of the template to a higher dielectric contrast. As has been previously mentioned, one possible use of the manufactured template, even without a complete gap, is the manufacture of devices that take advantage of the strong dispersion that electromagnetic radiation experiences in woodpile

structures of lower index of refraction. The exploration of this particular application would be a relatively small feat if the physics driving the process is detailed. Then a coherent broadband or variable source with a light intensity meter would suffice to validate this claim for the current template.

APPENDIX A

UNION OPERATION FOR OBJECTS

Since the union operation is not a mathematically sound operation for vectors and objects, its equivalent needs to be found. To begin, cylinder 1 is defined as C_1 , and cylinder 2 as C_2 . The permittivity function is rewritten in terms of these as,

$$\begin{aligned}
 C_1 &= \sum_{\bar{r}} \prod (h - |y' - \bar{R}z|) \prod (Rc - |p' - p_1 - \bar{R}p|) \\
 C_2 &= \sum_{\bar{r}} \prod (h - |y' - \bar{R}z|) \prod (Rc - |p' - p_2 - \bar{R}p|) \\
 \varepsilon(\bar{r}) &= \varepsilon_b + (\varepsilon_a - \varepsilon_b)[C_1 \cup C_2]
 \end{aligned}$$

The summation can be ignored since its function is to reproduce a crystal composed of these units. So, what remains is the product of two step functions describing the shape of the object in three-dimensional space. In the y' -direction, it is simply a square wave that specifies the starting and ending of the cylinders. In the $x''z''$ -directions, the step function is revolved about the center to give a circularly symmetric square wave; it is basically the circ function.

To create a composite structure from a cylinder and a rotated and displaced version of itself, addition will not give the correct result. With a little topological reshaping, the mathematical equivalent of the union operation is obtained. The cylinders, C_1 and C_2 , without

the multiplicative coefficients are of unit height. This is not a dimensional unit as the cylinders do have a length and a radius that is not unity. The value that the objects take is unity, similar to a one dimensional square wave of unit height.

The cylinders are inverted so that the space containing them is of height one and the cylinders are of height zero. Now, the product of the inverted cylinders will evaluate to zero everywhere that the cylinders exist, including their overlap. By subtracting this result from unity, the union operation is performed. Finally, with a little algebra and multiplying it by a constant and then adding another constant, the mathematical treatment of the composite structure is obtained.

$$\begin{aligned}
 \varepsilon(\bar{r}) &= \varepsilon_b + (\varepsilon_a - \varepsilon_b)[1 - (1 - C_1)(1 - C_2)] \\
 &= \varepsilon_b + (\varepsilon_a - \varepsilon_b)[1 - 1 + C_1 + C_2 - C_1 \times C_2] \\
 \varepsilon(\bar{r}) &= \varepsilon_b + (\varepsilon_a - \varepsilon_b)[C_1 + C_2 - C_1 \times C_2]
 \end{aligned}$$

APPENDIX B

MATLAB CODE THAT PREDICTS THE GEOMETRY OF THE STRUCTURE

```
%Code calculating the interference pattern resulting from two exposures
clear all
clc
tic

angle = 60;    %amount of rotation of the second exposure
shift = 0;    %amount of rotation of the coordinate system
zoff = 1.3;    %amount of translation in the z direction, C/4
%angle of first order diffraction in SU-8 mixture using n = 1.67
firstorder = 19.8;

lamb = .5145/1.67;

%The span and spacing of the limits and axes considered in micrometers
x = (0:.05:2.6);
y = (0:.05:2.6);
z = (1:.1:7.9);

%Generating the grid of points to work on
[X Y Z] = ndgrid(x,y,z);

%Specifying the know values of the k-vectors
k1 = 2*pi/lamb; k2 = k1; k3 = k1; k4 = k1; k5 = k1; k6 = k1;
k1x = 0; k1y = 0; k1z = k1;
k4x = 0; k4y = 0; k4z = k1;

%Specifying the amplitudes of the plane waves, obtained by measurement
E1o=0.68;
E2o=.335;
E3o=.335;
```

```

E4o=E1o;
E5o=.335;
E6o=.335;

%finding the remaining k-vectors
%first exposure
%%%%%%%%%%%%%%%%%%%%%%%%%%%%%%%%%%%%%%%%%%%%%%%%%%%%%%%%%%%%%%%%%%%%%%%%
%k-vector geometry for k2
theta = (shift)*pi/180;
phi = (90-firstorder)*pi/180;
%the function sph2cart converts from spherical to Cartesian
% returning its corresponding x y z components
[k2x,k2y,k2z] = sph2cart(theta,phi,k2);

%k-vector geometry for k3
theta = (shift)*pi/180;
phi = (90+firstorder)*pi/180;
[k3x,k3y,k3z] = sph2cart(theta,phi,k3);
%%%%%%%%%%%%%%%%%%%%%%%%%%%%%%%%%%%%%%%%%%%%%%%%%%%%%%%%%%%%%%%%%%%%%%%%

%second exposure
%%%%%%%%%%%%%%%%%%%%%%%%%%%%%%%%%%%%%%%%%%%%%%%%%%%%%%%%%%%%%%%%%%%%%%%%
%k-vector geometry for k5
theta = (shift+angle)*pi/180;
phi = (90-firstorder)*pi/180;
[k5x,k5y,k5z] = sph2cart(theta,phi,k5);

%k-vector geometry for k6
theta = (shift+angle)*pi/180;
phi = (90+firstorder)*pi/180;
[k6x,k6y,k6z] = sph2cart(theta,phi,k6);
%%%%%%%%%%%%%%%%%%%%%%%%%%%%%%%%%%%%%%%%%%%%%%%%%%%%%%%%%%%%%%%%%%%%%%%%

%Expressing the plane waves on the grid of points
E1 = E1o*exp(i*(k1x*X+k1y*Y+k1z*Z));
E2 = E2o*exp(i*(k2x*X+k2y*Y+k2z*Z));
E3 = E3o*exp(i*(k3x*X+k3y*Y+k3z*Z));
E4 = E4o*exp(i*((k4x*X+k4y*Y+k4z*(Z-zoff))));
E5 = E5o*exp(i*((k5x*X+k5y*Y+k5z*(Z-zoff))));
E6 = E6o*exp(i*((k6x*X+k6y*Y+k6z*(Z-zoff))));

%Electric fields of the first and second exposure
E1t = (E1+E2+E3);
E2t = (E4+E5+E6);

```

```

%The intensity distributions of the two exposures
I1t = abs(E1t).^2;
I2t = abs(E2t).^2;
It = I1t+I2t;

%Normalizing the intensities
It=It./max(max(max(It)));
I1t=I1t./max(max(max(I1t)));
I2t=I2t./max(max(max(I2t)));

%setting the normalized intensity value separating used and unused regions
level = 0.5;

%Preparing to plot, the data is smoothed to appear continuous in the plots
figure(1)
data = smooth3(It, 'gaussian',5);
p1 = patch(isosurface(x,y,z,data,level), ...
    'FaceColor',[0 0 150/255], 'EdgeColor','none');

p2 = patch(isocaps(x,y,z,data,level), ...
    'FaceColor','interp', 'EdgeColor','none');
isonormals(x,y,z,data,p1)

colormap 'jet';
view(139,15)
axis equal;
camlight headlight; lighting phong; material dull;
xlabel('X(um)'); ylabel('Y(um)'); zlabel('Z(um)');

%Title of the plot
title('Normalized Intensity')
axis([min(x) max(x) min(y) max(y) min(z) max(z)]);
colorbar

```

APPENDIX C

MATLAB CODE THAT SOLVES FOR THE DISPERSION RELATION

```
%Code that solves for the Eigenvalues of a three-dimensional periodic  
%dielectric lattice
```

```
clear all  
clc  
tic
```

```
n=3; %number of atoms in one axis direction  
NPW=(2*n+1)^3; %the number of plane waves to be used
```

```
epsa=13; %permittivity of the material  
epsb=1; %permittivity of the background  
a = 1; %periodicity a in the x and y directions  
c = 1.8; %periodicity in the stacking(z) direction  
R = a/8; %radius of the rods  
ae = R; %radius of the rods along the stacking direction  
be = c/8; %radius of the rods along the x and y directions  
h = a/sqrt(2); %the length of the rods, depends on orientation  
beta1 = pi/2-pi/4; %the angle of rotation of the first cylinder  
beta2 = -pi/4; %the angle of rotation of the second cylinder
```

```
%regular fcc vectors for a 90 degree woodpile structure
```

```
a1=1/2*[0 a c];  
a2=1/2*[a 0 c];  
a3=1/2*[a a 0];
```

```
%30 degree woodpile vectors
```

```
% a1 = [0 cos(15*pi/180)*a c/2];  
% a2 = [sin(15*pi/180)*a 0 c/2];
```

```

% a3 = [sin(15*pi/180)*a cos(15*pi/180)*a 0];

% 60 degree woodpile vectors
% a1 = [0 sqrt(3)*a/2 c/2];
% a2 = [a/2 0 c/2];
% a3 = [a/2 sqrt(3)*a/2 0];

% reciprocal lattice vectors
volume=dot(a1,cross(a2,a3));
b1=2*pi*cross(a2,a3)/volume;
b2=2*pi*cross(a3,a1)/volume;
b3=2*pi*cross(a1,a2)/volume;

% forming a 3D grid of integral spacing representing atoms
[Xgrid Ygrid Zgrid] = ndgrid(-n:n);
% forming the reciprocal space vectors
Gx=b1(1)*Xgrid + b2(1)*Ygrid + b3(1)*Zgrid;
Gy=b1(2)*Xgrid + b2(2)*Ygrid + b3(2)*Zgrid;
Gz=b1(3)*Xgrid + b2(3)*Ygrid + b3(3)*Zgrid;

% preparing the reciprocal space vectors for conversion to 2D
% creating the reciprocal space vectors G and G' by use of transpose
Gxm = repmat(Gx(:)',NPW,1);
Gym = repmat(Gy(:)',NPW,1);
Gzm = repmat(Gz(:)',NPW,1);

% reciprocal lattice vector G'
Gxn = Gxm';
Gyn = Gym';
Gzn = Gzm';

% 2D reciprocal space vectors, by mathematical operation (G-G')
Ggx = Gxm-Gxn;
Ggy = Gym-Gyn;
Ggz = Gzm-Gzn;

% Creating the various forms of reciprocal space vectors that will be used
G = horzcat(Gx(:),Gy(:),Gz(:));
clear Xgrid Ygrid Zgrid Gxm Gxn Gym Gyn Gzn Gzm Gx Gy Gz

Gx1 = Ggx*cos(beta1) + Ggy*sin(beta1);
Gy1 = -Ggx*sin(beta1) + Ggy*cos(beta1);

Gx2 = Ggx*cos(beta2) + Ggy*sin(beta2);
Gy2 = -Ggx*sin(beta2) + Ggy*cos(beta2);

```

```
Gp1 = sqrt((ae*Gy1).^2+(be*Ggz).^2);
Gp2 = sqrt((ae*Gy2).^2+(be*Ggz).^2);
```

```
Gr = sqrt((Ggx).^2+(Ggy).^2+(Ggz).^2);
Gg = horzcat(Ggx(:),Ggy(:),Ggz(:));
```

```
%eliminating division by 0 by replacing zero values with 1
```

```
na = find(Gr==0);
Gr(na) = 1;
```

```
na1 = find(Gp1==0);
Gp1(na1) = 1;
```

```
na2 = find(Gp2==0);
Gp2(na2) = 1;
```

```
clear Ggx Ggy Ggz
```

```
display('Calculating the permittivity, eps(G-G)');
r1=[a/8 a/8 2*be]; %position of the first cylinder
r2=[0 0 0]; %position of the second cylinder
```

```
%this part prepares a matrix to represent the dot product in the
%exponential terms due to displacement expressed by exp(i*r(1,2) dot G)
%dot product equivalent for the position of the first cylinder
r11 = repmat(r1,NPW^2,1);
dt1 = dot(Gg,r11,2);
dt1 = reshape(dt1,NPW,NPW);
```

```
%dot product equivalent for the position of the second cylinder
r22 = repmat(r2,NPW^2,1);
dt2 = dot(Gg,r22,2);
dt2 = reshape(dt2,NPW,NPW);
```

```
%fractional volume of the elementary cell
fr=pi*h*R*R/volume;
```

```
%forming the permittivity matrix
```

```
%%%%%%%%%%%%%%%%%%%%%%%%%%%%%%%%%%%%%%%%%%%%%%%%%%%%%%%%%%%%%%%%%%%%%%%%%
```

```
%the permittivity matrix for cylinder one
```

```
epsC1 = 2*fr*(epsa-epsb)*(sinc(Gx1*h/2).*besselj(1,Gp1)./(Gp1)).*exp(i*dt1);
```

```
%the permittivity matrix for cylinder two
```

```
epsC2 = 2*fr*(epsa-epsb)*(sinc(Gx2*h/2).*besselj(1,Gp2)./(Gp2)).*exp(i*dt2);
```

```

%the permittivity for the entire elementary cell
eps = epsC1+epsC2;
%amending the height at zeroes
eps(na) = epsb + 2*(epsa-epsb)*fr;

%forming the permittivity matrix for the overlapping case
% C1 = 2*fr*(sinc(Gx1*h/2).*besselj(1,Gp1)/(Gp1)).*exp(i*dt1);
% C2 = 2*fr*(sinc(Gx2*h/2).*besselj(1,Gp2)/(Gp2)).*exp(i*dt2);

% c1 = ifftn(C1);
% c2 = ifftn(C2);
% cc = (epsa-epsb).*(c1+c2-c1.*c2);
% eps = fftn(cc);
%
%or another way that avoids taking the inverse FFT
%% eps = (epsa-epsb)*(C1+C2-conv(C1,C2,'same'));
% eps(na) = epsb+(epsa-epsb)*(2*fr-fr^2);
%%%%%%%%%%%%%%%%%%%%%%%%%%%%%%%%%%%%%%%%%%%%%%%%%%%%%%%%%%%%%%%%%%%%%%%%

clear Gg Gr Gp1 Gp2 Gx1 Gx2 Gy1 Gy2 ep1 ep2 r11 r22 dt1 dt2 Ggx Ggy Ggz...
na na1 na2

%getting the inverse of the permittivity matrix, kappa
kappa = inv(eps);

clear eps

%preparing the k-vectors on the edge of the first Brillouin Zone
%k-vectors along which calculations are performed for a 90 degree structure
k1=interpolate([0 0.5 0.5]*[b1;b2;b3],...
[0.25 0.625 0.625]*[b1;b2;b3],4,0); %X to U
k2=interpolate([0.25 0.625 0.625]*[b1;b2;b3],...
[0.5 0.5 0.5]*[b1;b2;b3],4,0); %U to L
k3=interpolate([0.5 0.5 0.5]*[b1;b2;b3],...
[0 0 0]*[b1;b2;b3],4,0); %L to Gamma
k4=interpolate([0 0 0]*[b1;b2;b3],...
[0.25 0.5 0.75]*[b1;b2;b3],4,0); %Gamma to W
k5=interpolate([0.25 0.5 0.75]*[b1;b2;b3],...
[0.375 0.375 0.75]*[b1;b2;b3],4,0); %W to K
k6=interpolate([0.375 0.375 0.75]*[b1;b2;b3],...
[0.5 0.5 0]*[b1;b2;b3],4,0); %K to X'
k7=interpolate([0.5 0.5 0]*[b1;b2;b3],...
[0.625 0.625 0.25]*[b1;b2;b3],4,0); %X' to U'
k8=interpolate([0.625 0.625 0.25]*[b1;b2;b3],...
[0.5 0.75 0.25]*[b1;b2;b3],4,0); %U' to W'
k9=interpolate([0.5 0.75 0.25]*[b1;b2;b3],...

```

```

    [0.375 0.75 0.375]*[b1;b2;b3],4,0);          % W' to K'
k10=interpolate([0.375 0.75 0.375]*[b1;b2;b3],...
    [0.25 0.75 0.5]*[b1;b2;b3],4,1);          % K' to W''
kt=[k1;k2;k3;k4;k5;k6;k7;k8;k9;k10];

%% %The function created to expand the list of k vector by linear
%% %interpolation
% function kvector = interpolate(kstart,kend,n,ending)
%   kvector = zeros(n+1,3);
%   increment = (kend-kstart)/n;
%   for i=1:3
%       if increment(i) == 0
%           kvector(:,i) = 0;
%       else
%           rowvec = kstart(i):increment(i):kend(i);
%           kvector(:,i) = rowvec';
%       end
%   end
%   if ending == 0
%       kvector(n+1,:) = [];
%   %   temp = kvector(1:n,1:3);
%   %   clear kvector
%   %   kvector = temp;
%   %   clear temp
%   end

clear k1 k2 k3 k4 k5 k6 k7 k8 k9 k10

% *****
% Solving for the Eigenvalues
Eigen_freqs = [];
display('Solving the Hermitian Eigensystem for the Eigenvalues');
for i=1:size(kt,1)

    k=kt(i,:);
    K(:,1)=k(1)+G(:,1);
    K(:,2)=k(2)+G(:,2);
    K(:,3)=0;

    % the unit vectors e1 and e2 are found
    % e1 can be written in normalized form along (y,-x)
    magK = sqrt(K(:,1).^2+K(:,2).^2+K(:,3).^2);
    e1=[K(:,2)./magK,-K(:,1)./magK,zeros(length(K),1)];
    % eliminating division by zero
    e1(isnan(e1))=1/sqrt(2);

```

```

%reconfiguring K in the z direction
K(:,3)=k(3)+G(:,3);

%finding e2 such that it is normal to e1 and K
e2=cross(e1, K);
%normalizing e2 to unity
mage2 = sqrt(e2(:,1).^2+e2(:,2).^2+e2(:,3).^2);
mage22 = repmat(mage2,1,3);
e2=e2./mage22;

%eliminating division by zero
e2(isnan(e2))=1/sqrt(2);

%true magnitude of K
mK = sqrt(K(:,1).^2+K(:,2).^2+K(:,3).^2);

%forming the matrices given by the matrix form of the wave equation
M1=(mK.*e2(:,1),mK.*e2(:,2),mK.*e2(:,3))...
*[mK.*e2(:,1),mK.*e2(:,2),mK.*e2(:,3)]'.*kappa;
M3=(mK.*e2(:,1),mK.*e2(:,2),mK.*e2(:,3))...
*[mK.*e1(:,1),mK.*e1(:,2),mK.*e1(:,3)]'.*kappa;
Mt=[M1,M3];

clear M1 M3 mage2 mage22

M2=(mK.*e1(:,1),mK.*e1(:,2),mK.*e1(:,3))...
*[mK.*e2(:,1),mK.*e2(:,2),mK.*e2(:,3)]'.*kappa;
M4=(mK.*e1(:,1),mK.*e1(:,2),mK.*e1(:,3))...
*[mK.*e1(:,1),mK.*e1(:,2),mK.*e1(:,3)]'.*kappa;
M=[Mt;M2,M4];

clear Mt M2 M4 e1 e2 mk

% solving the eigen values of the total matrix M
% the eigen values are sorted to facilitate truncation to the lowest
% order modes
E=sort(abs(eig(M)));
% the Eigenvalues are adjusted to proper units, a/lambda or wa/(2pi*c)
Eigen_freqs(:,i)=sqrt(E(1:10)).*a./(2*pi);

display([horzcat('k',num2str(i)) ' of '...
horzcat('k',num2str(length(kt))) ' is done']);
toc
clear M E
end

```

```

%*****
% Plotting the Dispersion Relation
figure1 = figure;

% Create axes
axes1 = axes('Parent',figure1,...
    'XTickLabel',{'X','U','L','Gamma','W','K','X''','U''','W''''',...
    'K''','W'''''},'XTick',1:4:length(kt));
xlim([1 length(kt)]);
box('on');
grid('on');
hold('all');

% Create multiple lines using matrix input to plot
plot(1:length(kt),Eigen_freqs,'LineWidth',2,'Parent',axes1);

% Create title
title('Dispersion relation of a 90 degree woodpile photonic crystal');

% Create xlabel
xlabel('wave vectors k');

% Create ylabel
ylabel('wa/2\pic');

```

APPENDIX D

SAMPLE MPB CODE USED FOR THE PREDICTION OF THE DISPERSION RELATIONS

;MPB code that calculates the dispersion relation of a woodpile
;structure composed of either rectangular or cylindrical rods
;the sample code calculates for a structure with a C/L ratio of 1

;setting up the geometry and the dimensions of the basis
(set! geometry-lattice (make lattice
 (basis-size (sqrt 0.5) (sqrt 0.5) (sqrt 0.5))
 (basis1 0 1 1)
 (basis2 1 0 1)
 (basis3 1 1 0)))

;defining the k-vectors along which calculations are performed
(define-param k-interp 4)
(define X (vector3 0 0.5 0.5))
(define U (vector3 0.25 0.625 0.625))
(define L (vector3 0.5 0.5 0.5))
(define Gamma (vector3 0 0 0))
(define W (vector3 0.25 0.5 0.75))
(define K (vector3 0.375 0.375 0.75))
(define X' (vector3 0.5 0.5 0))
(define U' (vector3 0.625 0.625 0.25))
(define W' (vector3 0.5 0.75 0.25))
(define K' (vector3 0.375 0.75 0.375))
(define W'' (vector3 0.25 0.75 0.5))

;setting the order of the k-points and linearly interpolating
;between them to increase the resolution of the calculations
(set! k-points (interpolate k-interp (list X U L Gamma W K X' U' W' K' W'')))

```
(define-param eps 13) ; the dielectric constant of the material
(define diel (make dielectric (epsilon eps)))
```

```
(define-param h 0.25) ; height of logs
```

```
;creating the primitive cell
```

```
(define (first-gap w)
```

```
(set! geometry
```

```
(list
```

```
(make block (material diel)
```

```
(center (cartesian->lattice (0 0 0)))
```

```
(e1 (cartesian->lattice (1 1 0)))
```

```
(e2 (cartesian->lattice (1 -1 0)))
```

```
(e3 (cartesian->lattice (0 0 1)))
```

```
(size infinity w h))
```

```
(make block (material diel)
```

```
(center (cartesian->lattice (0.125 0.125 h)))
```

```
(e1 (cartesian->lattice (1 1 0)))
```

```
(e2 (cartesian->lattice (1 -1 0)))
```

```
(e3 (cartesian->lattice (0 0 1)))
```

```
(size w infinity h))))
```

```
(set! resolution 16) ;sets the resolution of the spatial grid
```

```
(set! num-bands 10) ;the number of bands to calculate for
```

```
(set! mesh-size 7) ; sets the size of the mesh
```

```
(run)
```

```
(retrieve-gap 2)) ; return the gap from band 1 to band 2
```

```
;maximizing the gap with respect to the width or the radius of the logs
```

```
(define result (maximize first-gap 0.1 0.02 0.5))
```

```
(print "width at maximum: " (max-arg result) "\n")
```

```
(print "gap size at maximum: " (max-val result) "\n")
```

```
;if instead cylinders are used, the later part of the code is
```

```
;replaced by the following
```

```
;(define (first-gap r)
```

```
;(set! geometry
```

```
; (list
```

```
; (make cylinder (material diel)
```

```
; (center (cartesian->lattice (0 0 0)))
```

```
; (axis (cartesian->lattice (1 1 0)))
```

```
; (radius r)
```

```

;      (height infinity))
;      (make cylinder (material diel)
;      (center (cartesian->lattice (0.125 0.125 h)))
;      (axis (cartesian->lattice (1 -1 0)))
;      (radius r)
;      (height infinity))))

;(set! resolution 16)
;(set! num-bands 10)
;(set! mesh-size 7) ; increase from default value of 3
;(run)

;(retrieve-gap 2) ; return the gap from TM band 1 to TM band 2

;(define result (maximize first-gap 0.05 0.02 0.3))
;(print "radius at maximum: " (max-arg result) "\n")
;(print "gap size at maximum: " (max-val result) "\n")

```

BIBLIOGRAPHY

1. J. W. S. Rayleigh, "On the remarkable phenomenon of crystalline reflexion described by Prof. Stokes", *Philosophical Magazine* 26, 256–265 (1888).
2. S. John, "Strong localization of photons in certain disordered dielectric superlattices", *Physical Review Letters* **58**, (23) 2486–2489 (1987).
3. E. Yablonovitch, "Inhibited Spontaneous Emission in Solid-State Physics and Electronics", *Physical Review Letters* 58, (20) 2059–2062 (1987).
4. T. F. Krauss, R. M. DeLaRue, S. Brand, "Two-dimensional photonic-bandgap structures operating at near-infrared wavelengths", *Nature* **383**, (6602): 699–702 (1996).
5. Review: S. Johnson (MIT) [Lecture 3: Fabrication technologies for 3d photonic crystals, a survey](#).
6. K.-M. Ho, C. T. Chan, C. M. Soukoulis, R. Biswas, and M. Sigalas, "Photonic band gaps in three dimensions: new layer-by-layer periodic structures", *Solid State Communications* 89, 413-416 (1994).
7. A. Hynninen, J. H. J. Thijssen, E. C. M. Vermolen, M. Dijkstra, and A. V. Blaaderen, "Self-assembly route for photonic crystals with a bandgap in the visible region", *Nature Materials* **6**, 202 -205 (2007).
8. M. Deubel, G. V. Freymann, M. Wegener, S. Pereira, K. Busch, C. M. Soukoulis, "Direct laser writing of three-dimensional photonic-crystal templates for telecommunications", *Nature Materials* 3, 444-447 (2004).
9. O. Toader, T. Y. M. Chan, and S. John, "Photonic Band Gap Architectures for Holographic Lithography", *Physical Review Letters* 92, 043905 (2004).
10. M. Campbell, D.N. Sharp, M.T. Harrison, R.G. Denning and A.J. Turberfield, "Fabrication of Photonic Crystals for the visible spectrum by Holographic Lithography", *Nature* **404**, 53 (2000).
11. S. Yang, M. Megens, J. Aizenberg, P. Wiltzius, P. M. Chaikin, and W. B. Russel, "Creating Periodic Three-Dimensional Structures by Multibeam Interference of Visible Laser", *Chemistry of Materials* 14, 2831 (2002).

12. I. Diviliansky, T. S. Mayer, K. S. Holliday, and V. H. Crespi, "Fabrication of Three-Dimensional Polymer Photonic Crystal Structures using Single Diffraction Element Interference Lithography", *Applied Physics Letters* 82, 1667 – 1669 (2003).
13. Y. V. Miklyaev, D. C. Meisel, A. Blanco, G. V. Freymann, K. Busch, W. Koch, C. Enkrich, M. Deubel, and M. Wegener, "Three-dimensional face-centered-cubic photonic crystal templates by laser holography: fabrication, optical characterization, and band-structure calculations", *Applied Physics Letters* 82, 1284 (2003).
14. Y. Lin, P. R. Herman, and K. Darmawikarta, "Design and holographic fabrication of tetragonal and cubic photonic crystals with phase mask: toward the mass-production of three-dimensional photonic crystals", *Applied Physics Letters* 86, 071117 (2005).
15. Yuankun Lin, David Rivera, and K. P. Chen, "Woodpile-type photonic crystals with orthorhombic or tetragonal symmetry formed through phase mask techniques", *Optics Express* 14, 887-892 (2006).
16. D. Chanda and P. R. Herman, "Phase tunable multilevel diffractive optical element based single laser exposure fabrication of three-dimensional photonic crystal templates", *Applied Physics Letters* 91, 061122 (2007).
17. N. Tetreault, G. V. Freymann, M. Deubel, M. Hermatschweiler, F. Perez-Willard, S. John, M. Wegener, and G. A. Ozin, "New route to three-dimensional photonic bandgap materials: silicon double inversion of polymer templates", *Advanced Materials* 18, 457-460 (2006).
18. J. Joannopoulos, S. Johnson, J. Winn, and R. Meade, "Photonic Crystals: Molding the Flow of Light", Second Edition, Princeton: Princeton University Press (2008).
19. H. Kosaka, T. Kawashima, A. Tomita, M. Notomi, T. Tamamura, T. Sato and S. Kawakami, "Superprism phenomena in photonic crystals", *Physical Review B*. 58, R10096 (1998).
20. H. Kosaka, T. Kawashima, A. Tomita, M. Notomi, T. Tamamura, T. Sato, and S. Kawakami, "Self-collimating phenomena in photonic crystals", *Applied Physics Letters* 74, 1212 (1999).
21. J. Serbin and M. Gu, "Superprism phenomena in polymeric woodpile structures", *Applied Physics Letters* 98, 123101 (2005).
22. Steven Johnson and John Joannopoulos, "Block-iterative frequency-domain methods for Maxwell's equations in a planewave basis", *Opt. Express* 8, 173-190 (2001).
23. J. Joannopoulos, R. Meade, and J. Winn, "Photonic Crystals: Molding the Flow of Light", Princeton University Press (1995).
24. Shangping Guo and Sacharia Albin, "Simple plane wave implementation for photonic crystal calculations", *Optics Express* 11, 167-175 (2003).

25. Ronald Bracewell, "The Fourier Transform and its Applications", McGraw Hill, Third Edition (1999).
26. R. Larson, B. Edwards, and D. Heyd, "Calculus", Sixth Edition, Houghton Mifflin Company (1998).
27. Wikipedia contributors, "Rotation matrix", Wikipedia, The Free Encyclopedia, http://en.wikipedia.org/w/index.php?title=Rotation_matrix&oldid=314531067 (accessed September 17, 2009).
28. Yuankun Lin, David Rivera, Zsolt Poole, and Kevin P. Chen, "Five-beam interference pattern controlled through phases and wave vectors for diamondlike photonic crystals", *Applied Optics* 45, 7971-7976 (2006).
29. Neil Ashcroft and David Mermin, "Solid State Physics", Thomson Learning (1976).
30. K. M. Ho, C. T. Chan, and C. M. Soukoulis, "Existence of a Photonic Gap in Periodic Dielectric Structures", *Physical Review Letters* 65, 3152 (1990).
31. Jun Hyuk Moon, Jamie Ford and Shu Yang, "Fabricating three-dimensional polymeric photonic structures by multi-beam interference lithography", *Polymers for Advanced Technologies* 17, 83–93 (2006).
32. Ngoc Diep Lai, Wen Ping Liang, Jian Hung Lin, Chia Chen Hsu, and Cheng Hsiung Lin, "Fabrication of two- and three-dimensional periodic structures by multi-exposure of two-beam interference technique", *Optics Express* **13**, 9605-9611 (2005).
33. Shu Yang, Mischa Megens, Joanna Aizenberg, Pierre Wiltzius, Paul. M. Chaikin, and William B. Russel, "Creating Periodic Three-Dimensional Structures by Multibeam Interference of Visible Laser", *Chemistry of Matererials*, 14 (7), pp 2831–2833 (2002)